**Department of Physics and Astronomy**
**Heidelberg University**

# Physics Reach of a Long-Lived ALP Detector at Belle II and ILC

Bachelor Thesis in Physics
submitted by

**Finn Tillinger**

born in Heidelberg (Germany)

**2021**

This Bachelor Thesis has been carried out by Finn Tillinger at the
Institute for Theoretical Physics Heidelberg
under the supervision of
Prof. Susanne Westhoff

## Abstract

In the search for long-lived particles, far detectors at colliders are an interesting concept to improve an experiment's sensitivity for their detection. In this thesis, we study the gains in sensitivity for the detection of long-lived axion-like particles given by different far-detector designs at the Belle II experiment and at the International Linear Collider. We show for both experiments that none of the far detectors provides significant improvements in sensitivity over the respective experiment's main detector. Furthermore, we find that the International Linear Collider is more sensitive for the detection of axion-like particles than Belle II. Nevertheless, only if both experiments feature an extensive axion-like particle search, the physics reach for them can be maximized.

## Zusammenfassung

Auf der Suche nach langlebigen Teilchen sind Far-Detektoren an Teilchenbeschleunigern ein interessantes Konzept, um die Sensitivität eines Experimets bezüglich deren Entdeckung zu erhöhen. In dieser Arbeit untersuchen wir den Zuwachs an Sensitivität bezüglich der Entdeckung von langlebigen Axion-like Particles, der durch verschiedene Far-Detektor Designs am Belle II Experiment und am International Linear Collider erreicht wird. Wir zeigen für beide Experimente, dass keiner der Far-Detektoren signifikante Verbesserungen der Sensitivität über den jeweiligen Hauptdetektor erbringt. Außerdem erschließen wir, dass der International Linear Collider eine bessere Sensitivität bezüglich der Entdeckung von Axion-like Particles als Belle II hat. Trotzdem sollten beide Experimente eine umfassende Axion-like Particle Suche durchführen, um die Wahrschenlichkeit einer Entdeckung zu maximieren.

# Contents

**Bibliography**

# 1 Introduction

The Standard Model of Particle Physics (SM) is the most comprehensive and experimentally best tested theory of particle physics. It comprises all known elementary particles and describes their interactions (without gravity). However, there are many phenomena which can not be explained by the Standard Model (e.g. dark matter and dark energy, neutrino-oscillations, g-factor of the muon, etc.), thus motivating physics beyond the Standard Model. A very popular type of such theories of new physics are extensions to the Standard Model featuring new particles. Because no such particles have been detected yet at any collider, these particles must be very weakly coupled to the other Standard Model particles making them long-lived.
The search for these long-lived particles (LLPs) at existing colliders is extremely challenging because the LLPs simply escape the detectors for sufficiently long decay lengths and therefore can solely be detected through missing energy signatures. One way to enhance the sensitivity for LLPs is the construction of so called far detectors, i.e. detectors which are positioned at larger distances to the interaction point and therefore can detect the decay of LLPs. An example is FASER [1] at the LHC which is expected to provide great gains in sensitivity for LLPs and will start operating in 2022 [2].

In this paper, we will investigate axion-like particles (ALPs), which are one sort of LLPs featured in several extensions of the SM (see Section 2.1), and the possible gains in sensitivity for their detection given by far detectors at the Belle II experiment and at the International Linear Collider (ILC). This thesis is the follow-up to an already existing far-detector study at Belle II [3].
Both experiments use $e^+e^-$-collisions which leads to much cleaner environments than in hadron colliders like the LHC. This alone already makes Belle II and ILC very sensitive to LLPs and specifically ALPs in the case of this study. It therefore is highly interesting to investigate, whether far detectors can enhance these two experiments' sensitivities for the detection of ALPs even further.
For each of the two experiments, we propose different designs for possible far detectors, which will here be called GAZELLE (Approximately Zero-background Experiment for Long-Lived Exotics), and determine their projected reach for ALPs. It is this paper's goal to determine the gain in sensitivity for the detection of ALPs which the proposed far detectors would provide compared to the respective experiment's main detector. Additionally, we want to evaluate whether Belle II or the ILC is better suited for an extensive ALP search.

This paper is structured as follows: in Section 2.1, the ALP model that will be used in this study is described. In Section 2.2, the exact methodology of the analysis, i.e. how the quantities of interest are calculated and what they are used for, is explained. Chapters 3 and 4 deal with the Belle II experiment and the ILC separately. Both are organized identically: firstly, the respective experiment is described and the proposed GAZELLEs are specified (Sections 3.1,4.1); secondly, possible sources of backgrounds and how to reject them are commented on shortly (Sections 3.2,4.2); thirdly, the kinematic distributions of the used ALP data are examined in detail (Sections 3.3,4.3); and lastly, the actual far-detector analysis is carried out (Sections 3.4,4.4). In Chapter 5, we compare the sensitivities for the detection of ALPs of Belle II and ILC and evaluate, which of the two experiments is better suited for a dedicated ALP search. Finally, we conclude this paper in Chapter 6 by summarizing the results of the analyses.

# 2 Preliminaries

## 2.1 ALP Model

Axion-like particles (ALPs) appear in pseudoscalar extensions to the Standard Model of Particle Physics (SM) as a result of the spontaneous breaking of a global symmetry of the theory at a high energy scale $\Lambda$. Therefore, ALPs are pseudo Nambu-Goldstone bosons. The name axion-like particle is motivated from the QCD axion, which was introduced by Peccei and Quinn to resolve the strong CP-problem [4, 5, 6, 7]. In contrast to the very light QCD axion, ALPs don't necessarily resolve the strong CP-problem and their masses can span over several orders of magnitude [8]. As the ALP's interactions with SM-particles are suppressed by the inverse high energy scale $1/\Lambda$, they become long-lived.

The effective lagrangian for our ALP model including all the relevant couplings to SM-particles is given by [9, 10]

$$\mathcal{L}_{\text{ALP}} = \sum_f \frac{c_f}{2}\frac{\partial^\mu a}{\Lambda}\bar{f}\gamma_\mu\gamma_5 f + c_{WW}\frac{a}{\Lambda}\frac{\alpha_2}{4\pi}W^A_{\mu\nu}\widetilde{W}^{\mu\nu,A}, \tag{2.1}$$

with the axion a, the coupling $c_f$ of the ALP to fermions, the coupling to the weak gauge bosons $c_{WW}$, the weak coupling parameter $\alpha_2$ and the weak field tensor $W^A_{\mu\nu}$ and its dual tensor $\widetilde{W}^{\mu\nu,A}$.

For simplicity, we set only $c_e, c_\mu$ non-zero for the fermionic couplings with $c_e = c_\mu \equiv c_l$ and solely focus on the decay into electrons or muons (generally, also decays like e.g. $a \to \gamma\gamma$ are possible, but they will be neglected here). The decay of our ALP is then determined by [11]

$$\Gamma_{a\to l\bar{l}} = \frac{m_l^2}{8\pi}\left(\frac{c_l}{\Lambda}\right)^2\sqrt{m_a^2 - 4m_l^2} \qquad \text{with} \quad l = e, \mu \tag{2.2}$$

for $m_a \geq 2m_l$. From this, we get the total decay width $\Gamma$ by

$$\Gamma(m_a, c_l/\Lambda) = \begin{cases} \Gamma_{a\to e^-e^+}, & \text{if} \quad m_a < 2m_\mu \\ \Gamma_{a\to e^-e^+} + \Gamma_{a\to\mu^-\mu^+}, & \text{if} \quad m_a \geq 2m_\mu \end{cases} \tag{2.3}$$

and thus the decay length $c\tau$ as a function of the parameters $m_a$ and $c_l/\Lambda$:

$$c\tau_a(m_a, c_l/\Lambda) = \frac{\hbar c}{\Gamma(m_a, c_l/\Lambda)}. \tag{2.4}$$

So the decay of the ALP is entirely determined by the leptonic coupling $c_l$ in our simplified model. Note that this simplification will not change the general results of this analysis.

The creation of the ALP on the other hand is entirely determined by the other part of the lagrangian, i.e. the weak interaction with coupling $c_{WW}$. Here, we have to differentiate between the creation processes at Belle II and ILC because of the different center of mass energies (see Sections 3.1,4.1) and the thus different dominant channels.

### 2.1.1 ALP Production at Belle II

In Belle II, the ALPs are produced in B-meson decays: $B \to Ka$. The ALP is radiated off in the FCNC loop of the B-decay (see Figure 2.1). The decay width for this process is given by [3, 12]

$$\Gamma_{B\to Ka} = \frac{|g_{sb}|^2}{16\pi\Lambda^2}|f_0(m_a^2)|^2\frac{(m_B^2 - m_K^2)^2}{m_B}\sqrt{1 - \frac{(m_K + m_a)^2}{m_B^2}}\sqrt{1 - \frac{(m_K - m_a)^2}{m_B^2}}, \quad (2.5)$$

with the scalar hadronic form factor $f_0(m_a^2)$ at momentum transfer $q^2 = m_a^2$ [13, 3] and the effective coupling $g_{sb}$ of the ALP to the FCNC $b \to s$. This effective coupling can be expressed as a function of the fundamental coupling $c_{WW}$ by calculating the loop of the FCNC (see Figure 2.1b) [10]

$$g_{sb} = -V_{ts}^* V_{tb}\frac{3\alpha_t\alpha}{16\pi^2 s_w^2}\frac{1 - x_t + x_t \ln x_t}{(1 - x_t)^2} \times c_{WW} \quad (2.6)$$

with the CKM-matrix elements $V_{ts} = 0.0388$, $V_{tb} = 1.013$ [14], $\alpha_t = y_t^2/(4\pi)$ with the top-Yukawa coupling $y_t = 0.6626$, $s_w^2 = \sin^2\theta_W = 0.2312$ with the weak mixing angle $\theta_W$ [14] and $x_t = m_t^2/m_W^2$.

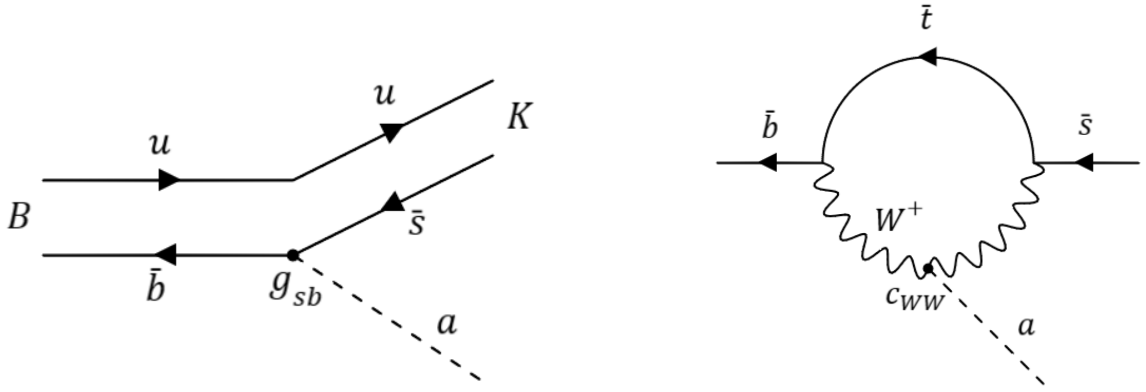

**(a)** $B \to Ka$ **(b)** FCNC Loop

**Figure 2.1:** Production of ALPs at Belle II

### 2.1.2 ALP Production at the ILC

At the ILC, the center of mass energy is high enough (see Section 4.1) that Z- and W-bosons can be produced in the electron-positron collisions with a high rate. The ALPs are then created in these processes through their coupling to the weak gauge bosons. In contrast to the Belle II part, we investigate four different production channels:
a) $e^+e^- \rightarrow a\gamma$ (Figure 2.2a), b) $e^+e^- \rightarrow ae^+e^-$ (Figure 2.2b), c) $e^+e^- \rightarrow a\nu\nu$ (Figure 2.2c) and d) $e^+e^- \rightarrow Z\gamma \rightarrow a\gamma\gamma$ (Figure 2.2d). Especially the last channel is interesting because the Z in the intermediate step is produced as on-shell particle, which gives higher rates (compared to channels (b) and (c); the rate for channel (a) is higher because it is a lower order diagram) and leads to different kinematic distributions for the ALPs (see Section 4.3).

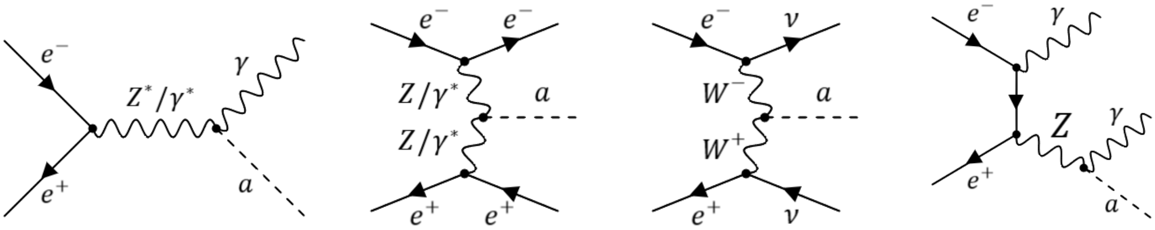

**(a)** $e^+e^- \rightarrow a\gamma$ **(b)** $e^+e^- \rightarrow ae^+e^-$ **(c)** $e^+e^- \rightarrow a\nu\nu$ **(d)** $e^+e^- \rightarrow a\gamma\gamma$

**Figure 2.2:** Production of ALPs at the ILC

## 2.2 Methodology of the Analysis

In this section, we discuss the methodology of the analysis, i.e. which quantities we want to determine and how they are being calculated.

### 2.2.1 Datasets

The basis from which we carry out the analysis is simulated data. For both experiments, Belle II and ILC, we can simulate ALP events where one event $i$ contains the ALP's mass $m_a$, the momentum $(p_x, p_y, p_z)$ and the ALP's production vertex $(x, y, z)$.
For Belle II, the events are simulated from the decay $B^+ \rightarrow K^+a$, where the $B^+$-meson originates from the main reaction at Belle II: $e^+e^- \rightarrow \Upsilon(4S)$ at $\sqrt{s} = 10.58\,\text{GeV}$ (see Section 3.1), using `EvtGen`. Respectively 10000 events are simulated for the ALP masses 0.05 GeV, 0.3 GeV, 1 GeV, 2 GeV and 4 GeV.
For the ILC, we simulate events for the different ALP production channels $e^+e^- \rightarrow a\gamma$, $e^+e^- \rightarrow ae^+e^-$, $e^+e^- \rightarrow a\nu\nu$ and $e^+e^- \rightarrow Z\gamma \rightarrow a\gamma\gamma$ (see Section 2.1) at $\sqrt{s} = 250\,\text{GeV}$ (see Section 4.1), using `MadGraph`. This is done solely for the mass 0.3 GeV because

the different masses from Belle II are all very small compared to ILC's center of mass energy and thus all have the same kinematic properties, which would ultimately result in the same qualitative results for different mass scenarios. Therefore, we keep the mass constant and rather focus on differences between the four production channels. 10000 events are simulated for each channel respectively.

### 2.2.2 Decay Probabilities

The first objective of the analysis is to determine the mean probabilities $\langle \mathbb{P} \rangle$ for ALPs to decay within a given detector volume as a function of the coupling $c_l/\Lambda$. As we assume 100% detection efficiency (see Section 3.1), this is equivalent to the mean probability for an ALP to be detected by the given detector.
The probability $\mathbb{P}_i$ for the ALP event $i$ to decay within a certain volume is given by the exponential decay law

$$\mathbb{P}_i(c_l/\Lambda) = \exp\left(-\frac{d_i^{in}}{\beta\gamma_i c\tau(c_l/\Lambda)}\right) - \exp\left(-\frac{d_i^{out}}{\beta\gamma_i c\tau(c_l/\Lambda)}\right), \tag{2.7}$$

where $d^{in}$ and $d^{out}$ denote the distances the ALP travelled before entering and exiting the detector (see Figure 2.3), $\beta\gamma$ denotes the Lorentz-boost and $\tau(c_l/\Lambda)$ is the lifetime of the ALP as given by Equation 2.4.

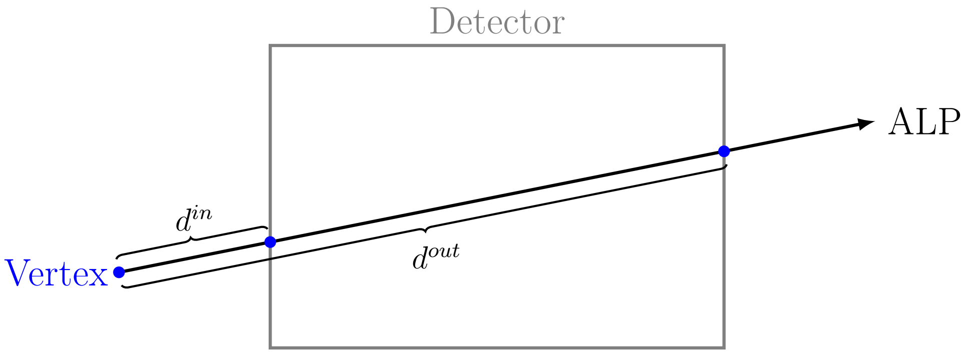

**Figure 2.3:** Schematic for the definition of $d^{in}$ and $d^{out}$

The distances $d^{in}$ and $d^{out}$ are determined by calculating the intersections of the line, created by the ALP vertex and the ALP momentum as direction, with the detector, i.e. the ensemble of all its faces. If there is no intersection for an event $i$, we set $d^{in}, d^{out} = 0$ because this gives $\mathbb{P}_i = 0$. If there is only one intersection, meaning that the ALP vertex lies within the detector, we set $d^{in} = 0$ and $d^{out}$ to be the distance between the vertex and the intersection point. If there are two intersections, $d^{in}$ and $d^{out}$ are defined as in Figure 2.3. The Lorentz-boost $\beta\gamma_i$ for the event $i$ is determined by $\beta\gamma_i = |\vec{p}_i|/m_a$. These $\mathbb{P}_i$ are calculated for all 10000 events for a given coupling $c_l/\Lambda$ and, for Belle II, a given mass $m_a$, or, for ILC, a given production channel, and from this the mean probability

$$\langle \mathbb{P} \rangle (c_l/\Lambda) = \frac{1}{N} \sum_{i=1}^{N} \mathbb{P}_i(c_l/\Lambda) \tag{2.8}$$

for an ALP with given coupling to be detected by a detector can be calculated.

An interesting case is the case of long decay lengths $l = \beta\gamma c\tau \gg d^{in}, d^{out}$. In this limit, the probability for an ALP to decay within a detector simplifies to (expansion of Equation 2.7 to first order)

$$\mathbb{P} \approx \frac{d^{out} - d^{in}}{l} \tag{2.9}$$

and thus the mean probability for ALPs to decay within a given detector is given by

$$\langle \mathbb{P} \rangle \approx \frac{\Omega}{4\pi} \times \frac{D}{l}, \tag{2.10}$$

where $\Omega$ is the detector's solid angle coverage and $D$ is the detector's mean radial thickness (note that this only holds if ALPs are emitted isotropically from the interaction point of the collisions, which is an acceptable approximation to first order). So the quantity $\Omega \times D$ entirely determines the probability for ALPs to decay within a detector in the long-decay-length-limit (and under our assumption of isotropy). Therefore, the quantity $\Omega \times D$ can give a first insight into a detector's sensitivity for the detection of long-lived ALPs.

### 2.2.3 Number of Detected ALPs

The second objective of the analysis is the calculation of the mean number $N_{dec}$ of expected detected ALP events for a given detector. With the zero-background assumption, we can proclaim the discovery of an ALP at 95% CL if we have $N_{dec} \geq 3$ [3]. So the region in parameter-space (e.g. $c_l/\Lambda$) which is defined by $N_{dec} \geq 3$ is the region where a given detector is sensitive to the discovery of ALPs. Thus, the determination of the quantity $N_{dec}$ is of central importance for the evaluation of the physics reach of our far detectors.
Below, different ways of calculating $N_{dec}$ in dependence of different parameters are described.

1. **$N_{dec}$ as a Function of $c_l/\Lambda$:**
   For Belle II, the mean number of detected ALP events can easily be determined using

   $$N_{dec}(c_l/\Lambda) = N_{B\overline{B}} \times \mathrm{Br}_{B\to Ka}(m_a, g_{sb}) \times \langle \mathbb{P} \rangle (c_l/\Lambda), \tag{2.11}$$

   where $N_{B\overline{B}} = 5 \times 10^{10}$ is the number of produced B-meson events at Belle II at an integrated luminosity of $50\,\mathrm{ab}^{-1}$ (goal for integrated luminosity at the Belle II experiment [15]), $\langle \mathbb{P} \rangle (c_l/\Lambda)$ is the mean probability for an ALP to be detected by a detector (see Equation 2.8) and $\mathrm{Br}_{B\to Ka}(m_a, g_{sb})$ follows directly from Equation 2.5. We take as numeric values for $g_{sb}$ the upper bounds, i.e. the maximum allowed values, from searches for $B \to K +$ invisible at BABAR [16]. They are enlisted in Table 2.1. In Equation 2.11 above should in principle be a factor of $\mathrm{Br}_{a\to l\bar{l}}$ as well because our GAZELLE detectors can solely detect leptonic decays. However, in our simple model this factor is simply $\mathrm{Br}_{a\to l\bar{l}} = 1$ as only leptonic decays are possible for our ALPs and thus this factor can be excluded.

| $m_a$ [GeV] | 0.05 | 0.3 | 1 | 2 | 4 |
|---|---|---|---|---|---|
| $g_{sb}$ | $3.95 \times 10^{-6}$ | $3.95 \times 10^{-6}$ | $3.91 \times 10^{-6}$ | $3.80 \times 10^{-6}$ | $3.47 \times 10^{-6}$ |

**Table 2.1:** Numeric values for $g_{sb}$ for different masses [16]

For the ILC, we calculate $N_{dec}$ slightly differently but of course the result will be completely equivalent:

$$N_{dec}(c_l/\Lambda) = \mathcal{L}_{ILC} \times \sigma(e^+e^- \to X) \times \langle \mathbb{P} \rangle (c_l/\Lambda). \tag{2.12}$$

Here, $\mathcal{L}_{ILC} = \int L_{ILC}\mathrm{d}t = 250\,\mathrm{fb}^{-1}$ is the goal for integrated luminosity of the ILC at $\sqrt{s} = 250\,\mathrm{GeV}$ [17], $\sigma(e^+e^- \to X)$ is the cross-section of a given ALP production channel which is given by `MadGraph` along with the simulated data and $\langle \mathbb{P} \rangle (c_l/\Lambda)$ again is the mean probability for an ALP to be detected by a given detector. Just as before, the factor of $\mathrm{Br}_{a\to l\bar{l}}$ has been discarded as it is equal one.

Having $N_{dec}$ as a function of just one parameter $c_l/\Lambda$, we can easily determine the lower bounds of sensitivity, i.e. the minimum value of $c_l/\Lambda$ with $N_{dec}(c_l/\Lambda) \geq 3$, for all our detectors. These lower bounds for all GAZELLEs can then be compared to the lower bound of the corresponding main detector (Belle II main detector or ILC main detector) and thus the gain in sensitivity of one given far detector over the main detector can be assessed.
Note that we could of course also determine the upper bounds, but this quantity is not of interest for far detectors because they are built to cover decay lengths as long as possible, i.e. couplings as low as possible.

2. **$N_{dec}$ as a Function of $c\tau$ and $\sigma$:**
In Equation 2.12, we can treat $\sigma(e^+e^- \to X)$ as a free parameter instead of inserting the fixed numeric values from `MadGraph` and we can easily convert the $c_l/\Lambda$-dependence in $\langle \mathbb{P} \rangle$ into a $c\tau$-dependence using Equation 2.4. Then, we obtain

$$N_{dec}(c\tau, \sigma) = \mathcal{L}_{ILC} \times \sigma \times \langle \mathbb{P} \rangle (c\tau), \tag{2.13}$$

so $N_{dec}$ as a function of two parameters $c\tau$ and $\sigma$. From this, we get regions in 2D parameter-space where $N_{dec} \geq 3$, which will be depicted in 2D Heatmaps (see e.g. Figure 4.9).
This dependence of $c\tau$ and $\sigma$ is more general and model-independent than the

former $c_l/\Lambda$-dependence and therefore, the results can be compared to other studies and ALP models more easily. This however will only be done for the ILC part of the analysis because the results in the preceding Belle II far-detector study [3] only have the former $c_l/\Lambda$-dependence and the Belle II part of this study is supposed to produce comparable results.

3. **$N_{dec}$ as a Function of $c_l/\Lambda$ and $c_{WW}/\Lambda$:**
   Finally, we want to determine $N_{dec}$ as a function of $c_l/\Lambda$ and the ALP's coupling to the W-bosons $c_{WW}$ for the two main detectors of the two experiments. Having this, one can easily compare the Belle II detector's sensitivity for ALPs to ILC's sensitivity. This comparison can not be done with $N_{dec}$ as a function of $c\tau$ and $\sigma$ as described before because the cross-section $\sigma$ describes two completely different reactions in the two experiments and thus can not be regarded as the same parameter. If we however boil down the results to the fundamental couplings of the ALP, we can directly compare Belle II to ILC.
   This of course is of major interest because it tells us, whether a long-lived ALP search program at ILC should be initiated or if Belle II's reach is already better and thus the search for long-lived ALPs can be done exclusively there.

   To calculate $N_{dec}$ in dependence of $c_l/\Lambda$ and $c_{WW}/\Lambda$ for Belle II, we start from Equation 2.11 and simply view $g_{sb}$ as a free parameter (instead of fixing it as before). $g_{sb}$ itself depends on $c_{WW}$ according to Equation 2.6. Inserting this into Equation 2.11, we get $N_{dec}$ in dependence of $c_l/\Lambda$ and $c_{WW}/\Lambda$.

   For the ILC, we start with Equation 2.12. We know that $\sigma(e^+e^- \to X) \propto (c_{WW}/\Lambda)^2$ and we realize that the events have been simulated with fixed $c_{WW}/\Lambda = 1\,\mathrm{TeV}^{-1}$, which means that the cross-section $\sigma_{\texttt{MadGraph}}$ given by `MadGraph` corresponds to $\sigma(c_{WW}/\Lambda = 1\,\mathrm{TeV}^{-1})$. Thus, we conclude

$$\sigma(c_{WW}) = c_{WW}^2 \times \sigma_{\texttt{MadGraph}}. \tag{2.14}$$

   Inserting this relation into Equation 2.12, we get $N_{dec}$ in dependence of $c_l/\Lambda$ and $c_{WW}/\Lambda$.

   To be then able to compare Belle II to the ILC, we must restrict the Belle II results to the 0.3 GeV ALP because this is the only ALP mass under consideration for the ILC. So for Belle II, we get $N_{dec}$ in dependence of $c_l/\Lambda$ and $c_{WW}/\Lambda$ once (the 0.3 GeV ALP) and for the ILC, we get $N_{dec}$ in dependence of $c_l/\Lambda$ and $c_{WW}/\Lambda$ four times (once per production channel).

# 3 Belle II

## 3.1 Detectors

In this section, we firstly discuss the experimental setup at the Belle II experiment and secondly the detector geometries which are going to be investigated.

The labframe's coordinate system is from here on defined as follows: the center $(0, 0, 0)$ coincides with the collision point of electron and positron, the $z$-axis coincides with the electron beam, the $y$-axis is orthogonal to the ground and points upwards and the $x$-axis is then determined by the other two axes. In this frame, spherical coordinates $(r, \theta, \phi)$ and cylindrical coordinates $(\rho, \phi, z)$ are defined as usual.

### 3.1.1 The Belle II Experiment

The Belle II experiment at KEK, the High Energy Accelerator Research Organization in Japan, aims at the precise investigation of B-meson physics to explore physics beyond the Standard Model. It is the follow-up experiment to the Belle experiment, which contributed to the discovery of CP-violation as predicted by the theory of Kobayashi and Maskawa [18, 19].

The collider for the Belle II experiment is the SuperKEKB. The SuperKEKB is a circular electron-positron collider (see Figure 3.1), where 7GeV electrons collide with 4GeV positrons. These beam energies result in a center of mass energy of $\sqrt{s} = 10.58\,\text{GeV}$, coinciding with the $\Upsilon(4\text{S})$ resonance, which nearly exclusively decays into B-mesons [14]. The SuperKEKB operates at a ultra-high luminosity of $L = 8 \times 10^{35}\,\text{cm}^{-2}\text{s}^{-1}$ and aims at accumulating an integrated luminosity of $\int L\text{d}t = 50\,\text{ab}^{-1}$ [15]. Due to the asymmetry in energies, all particles are boosted in the electron beam direction relative to the center of mass frame.

The Belle II detector is placed in Tsukuba Hall slightly underground. It is an arrangement of various subdetectors, cylindrically layered around the beam pipe (see Figure 3.2). A pixel detector (PXD) and silicon vertex detector (SVD) serve the purpose of precise tracking and thus the accurate reconstruction of vertices. The central drift chamber (CDC) further measures tracks but also particle's momenta and their energy loss due to ionization. This information plays a crucial role in particle identification. In detectors in the end-cap and barrel (PID), Cherenkov radiation along with timing information is used for particle identification. A calorimeter system (ECL) for energy measurements and spatial cluster information is installed. The outermost detector is a kaon and muon detector (KLM) which provides further measurements of $\mu$s and $K_L^0$s because these particles escape all previous inner detectors [19, 20, 21].

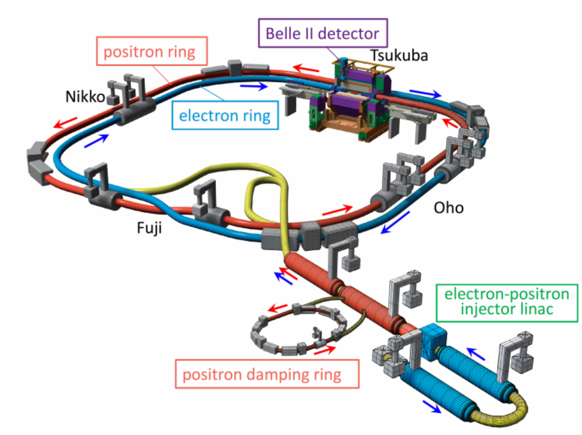

**Figure 3.1:** Schematic view of SuperKEKB; taken from [15]

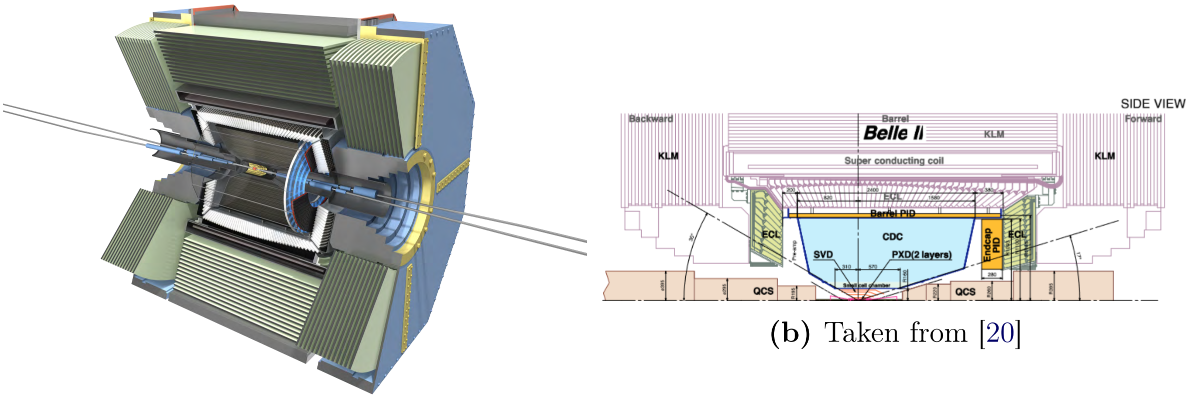

**(b)** Taken from [20]

**(a)** Taken from [22]

**Figure 3.2:** Schematic views of the Belle II detector

Throughout the entire analysis, the GAZELLE detectors and their performances will always be compared to the tracking detectors of the Belle II detector, which we will call CDC (although PXD and SVD are also included). For this CDC, we assume perfect detection efficiency of lepton-antilepton pairs from ALP decays in the range $z \in [-55\,\text{cm}, 140\,\text{cm}]$, $\theta \in [17°, 150°]$ and $\rho \geq 0.9\,\text{cm}$. The CDC then covers a solid angle of $\Omega = 11.45$ (91% angular coverage) and has a mean radial thickness of $D = 72.2\,\text{cm}$.

### 3.1.2 GAZELLE Detectors at Belle II

The task of the GAZELLE detectors is the measurement of the lepton-antilepton final state of an ALP decay. We want to be able to differentiate such ALP decays from backgrounds and to determine the invariant mass of the ALP. The content of the following paragraph is entirely summarized from and can be found in more detail in the preceding

Belle II far-detector study [3].

To achieve the aforementioned requirements, we need tracking of charged particles with timing information along the tracks. Calorimetry will not be crucially needed, which will reduce GAZELLE's expenses significantly. Such a detector could provide us with vertex positions, particle velocities $\beta$ and track directions from the time measurements along the tracks, the invariant mass of the ALP from velocities and the opening angle between the two tracks [23], the direction of the ALP track and timing information between activity in Belle II and GAZELLE. Especially the reconstructed ALP's track direction and the timing information between Belle II and GAZELLE can be used to reject backgrounds as the ALP track must point somewhere near the collision point and the Belle II detector must detect activity shortly before GAZELLE.
We will not specify the detector technology any further; however, we will assume 100% detection efficiency for ALP decays within the given detector volumes.

In our analysis, three new GAZELLE designs, Forward-GODZILLA, Top-GAZELLE and Roof-GODZILLA (the term GODZILLA refers to a GAZELLE design from [3]), will be investigated. Their performances will be compared to the CDC to examine potential gains over the Belle II detector and to L-GAZELLE from the preceding GAZELLE study [3], which had the best results there.

- **Forward-GODZILLA:**
  Forward-GODZILLA is a $(25 \times 10 \times 50)$m cuboid centered around $(-27, 18, 36)$m. Thus, Forward-GODZILLA is placed outside Tsukuba Hall on ground level, shifted in positive beam direction relative to the collision point. This position aims at detecting ALPs in the forward direction. It has a solid angle of $\Omega = 0.44$ (3.5% angular coverage) and a mean radial thickness of $D = 13.71\,\mathrm{m}$.

- **Top-GAZELLE:**
  Top-GAZELLE is a $(50 \times 4 \times 27)$m cuboid centered around $(13, 14, 0)$m. Thus, Top-GAZELLE is placed right underneath the whole ceiling of Tsukuba Hall above the Belle II detector. This position aims at detecting ALPs in transverse direction to the beam. It has a solid angle of $\Omega = 2.69$ (21.4% angular coverage) and a mean radial thickness of $D = 4.68\,\mathrm{m}$.

- **Roof-GODZILLA:**
  Roof-GODZILLA is a $(50 \times 10 \times 28)$m cuboid centered around $(15, 21, 0)$m. Thus, Roof-GODZILLA is placed on top of the ceiling of Tsukuba Hall above the Belle II detector. This position aims at detecting ALPs in transverse direction to the beam just like Top-GAZELLE. It has a solid angle of $\Omega = 2.02$ (16.1% angular coverage) and a mean radial thickness of $D = 9.38\,\mathrm{m}$. Conceptually, Top-GAZELLE and Roof-GODZILLA are very similar; however, it will be interesting to see, whether a closer distance to the collision point or a larger detector is more beneficial for sensitivity for the detection of long-lived ALPs.

- **L-GAZELLE:**
  L-GAZELLE consists of two detectors within Tsukuba Hall:

1. LG-B1:
   LG-B1 is a $(6 \times 16 \times 24)$m cuboid centered around $(35, 2.279, 0)$m. It has a solid angle of $\Omega = 0.34$ (2.7% angular coverage) and a mean radial thickness of $D = 5.25\,\mathrm{m}$.
2. LG-B2:
   LG-B2 is a $(26 \times 16 \times 8)$m cuboid centered around $(19, 2.279, 8)$m. It has a solid angle of $\Omega = 1.15$ (9.2% angular coverage) and a mean radial thickness of $D = 8.68\,\mathrm{m}$.

This design is supposed to be a mix of forward and transverse coverage and, as mentioned above, produced the best results in the preceding GAZELLE study [3].

To visualize the different geometries under study, schematics of the side- and topview of all detectors are given in Figure 3.3.

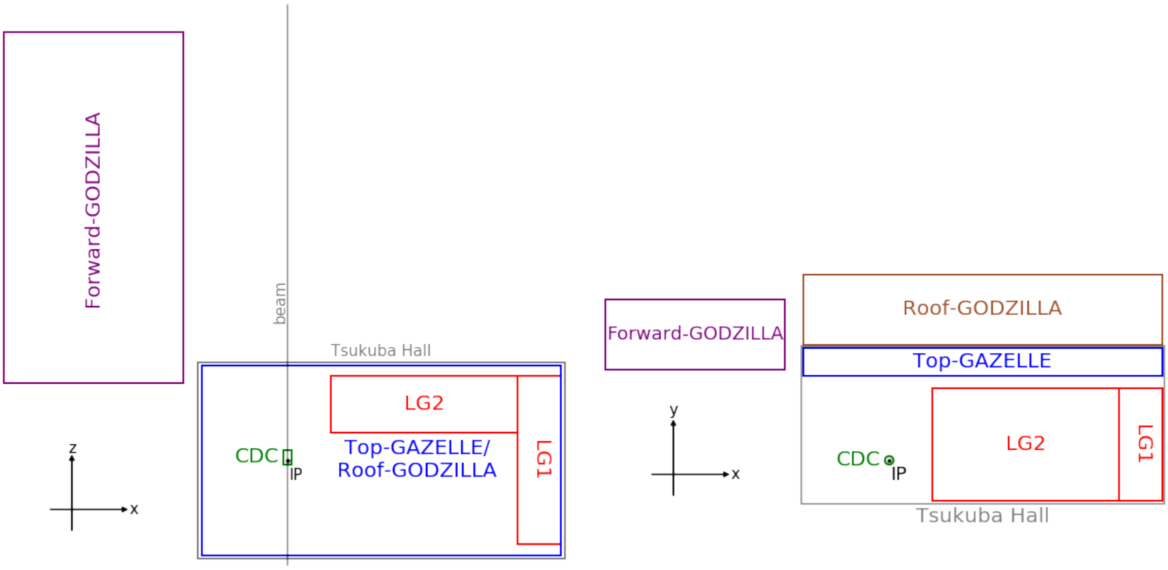

**(a)** Topview

**(b)** Sideview

**Figure 3.3:** Schematics of all detectors at Belle II

As we see in Equation 2.10, the quantity $D \times \Omega$ gives first insight into a detector's sensitivity in the long decaylength limit. Thus, these values are gathered for all detectors under study in Table 3.1.

| | CDC | FG | TG | RG | LG-B1 | LG-B2 |
|---|---|---|---|---|---|---|
| $\Omega$ | 11.45 | 0.44 | 2.69 | 2.02 | 0.34 | 1.15 |
| $D$ [m] | 0.72 | 13.71 | 4.68 | 9.38 | 5.25 | 8.68 |
| $\Omega \times D$ [m] | 8.24 | 6.03 | 12.59 | 18.95 | 1.76 | 10.0 |

**Table 3.1:** Solid angle, mean radial thickness and their product for all detectors

All proposed geometries are designed to not collide with existing major infrastructure like walls or electronics and thus should not require exceptional engineering. If built, the exact positions and sizes of the detectors of course can still vary.

## 3.2 Backgrounds

Any event which consists of two charged particles and thus giving us two tracks in a GAZELLE detector is a possible background event. In general, a background event can either originate from particles (directly or indirectly) created in the electron-positron collisions or from cosmic rays. In the following, we briefly discuss different sources of backgrounds and how to effectively reject them. All following information is entirely taken from and can be read in more detail in the preceding Belle II far-detector study [3].

### 3.2.1 $K_L^0$ Backgrounds

One possible source of backgrounds is $K_L^0$ mesons decaying within GAZELLE: $K_L^0 \to \pi^\pm + l^\mp + \nu$. There are three different ways how a $K_L^0$ can get into GAZELLE: direct kaons from the $e^+e^-$-collisions, indirect kaons which originate from the decay of primary muons and kaons which originate from the decay of cosmic muons.

1. **Direct $K_L^0$s:**
   Direct $K_L^0$ mesons from the collisions is a fairly unlikely source of background because they are usually completely absorbed in the Belle II detector. To get rid of those kaons escaping Belle II, shielding around the GAZELLE detector is an effective way to absorb these backgrounds.

2. **Indirect $K_L^0$s:**
   Indirect $K_L^0$ mesons is a much more likely source of backgrounds. Such kaons can be produced when primary muons (which penetrate Belle II completely) interact with e.g. shielding material or walls. These backgrounds can be rejected by tracking muons precisely in Belle II and using the time information between Belle II and GAZELLE.

3. **Cosmic $K_L^0$s:**
   $K_L^0$ mesons can also be produced when muons from cosmic rays interact with walls or shielding material. To reject such backgrounds, one can use that the reconstructed kaon's momentum will in general not coincide with the direction of the interaction point of the $e^+e^-$-collisions.

Of course, we get conceptually the same backgrounds if we replace the $K_L^0$ mesons above with other neutral hadrons which decay into two charged particles (e.g. $K_S^0$ or $\Lambda$). However, these are much more unlikely than the $K_L^0$-backgrounds as their lifetimes are much smaller and they therefore will mostly decay before reaching GAZELLE.

### 3.2.2 Muon Backgrounds

If tracking is not done accurately in GAZELLE, a muon decay can appear like two charged particles which then qualifies as a background event. We differentiate between primary muons from the collisions and cosmic muons.

1. **Primary Muons:**
   As discussed above, muons can penetrate the Belle II detector and therefore reach GAZELLE. Background rejection here follows the exact same idea as for indirect kaons.
2. **Cosmic Muons:**
   Muons from cosmic rays can appear in GAZELLE as a possible background. Background rejection follows the same idea as for cosmic kaons.

Because we have effective means for rejecting all different sorts of backgrounds, we will work with the zero-background assumption in the analysis. While this assumption will never be fully realized in experiments, the obtained results will still be useful and qualitatively true.

## 3.3 Kinematic Distributions

Before doing any detector analysis, it is useful to firstly investigate some basic kinematic distributions of our used ALP data. These distributions inspired the GAZELLE designs under study and they will help us to understand the results of the analysis.
Distributions of interest are the $\theta$-, $p_T$- and $E$-distribution, where $\theta$ denotes the polar angle of the ALP momentum, $p_T$ denotes the transverse momentum and $E$ the total ALP energy. All distributions are depicted in Figure 3.4.

One general observation from all three distributions is that the 4 GeV ALP differs from the other ALPs significantly, while the four lighter ALPs are very similar in all their distributions (just the 2 GeV ALP is slightly in-between).
One can clearly see in the $\theta$-distribution in Figure 3.4c that the heavy ALP is much more boosted in forward direction than the others, which are more evenly, though still slightly boosted in the forward direction, distributed over all possible directions. Practically no heavy ALP is emitted in backward direction. The 4 GeV ALP inherits more of the original CMS momentum (recall that the center of mass has a boost in positive z-direction in the labframe), while the lighter ALPs are less restricted in their directions. From this, we can conclude that a detector in forward direction might be the optimal choice to investigate heavy ALPs and a detector in transverse direction might be best for the lighter ALPs.

This conclusion is further reassured by the $p_T$-distribution in Figure 3.4a. Here, we see the exact same thing: the heavy ALP has a significantly smaller transverse momentum

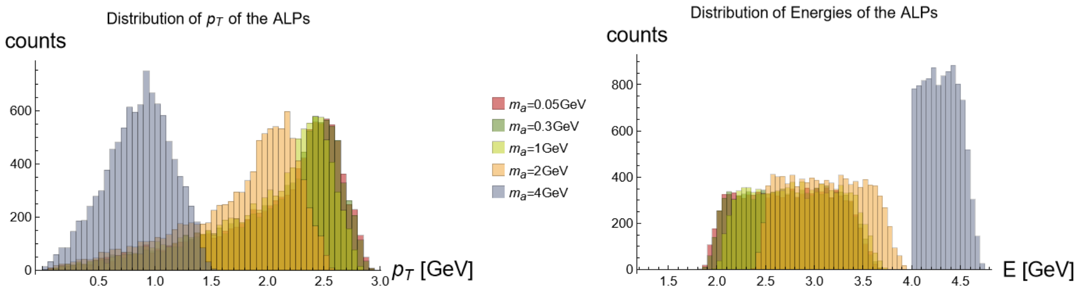

**(a)** $p_T$-distribution **(b)** $E$-distribution

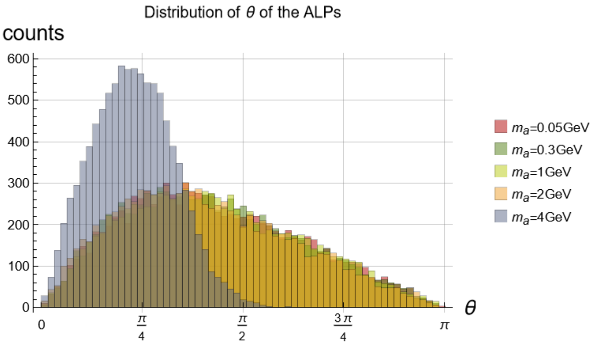

**(c)** $\theta$-distribution

**Figure 3.4:** Kinematic distributions of the ALP dataset

than the others, i.e. the heavy ALP will not be found in transverse direction but rather in longitudinal direction.
Lastly, the $E$-distribution in Figure 3.4b can be seen as a consistency check: all distributions start with the respective ALP mass, e.g. the $E$-distribution of the 4 GeV ALP solely has entries above 4 GeV. This of course is perfectly reasonable as a (free) particle's energy must be greater than its rest energy. So these distributions confirm that our used ALP data is free of obvious errors.

In conclusion, we see that a forward detector for heavy ALPs and a transverse detector for lighter ALPs is a sensible choice to maximize sensitivity. These thoughts together with practical limitations then motivated the GAZELLE designs discussed in Section 3.1.

## 3.4 Analysis

In this section, we carry out the detector analysis for the Belle II experiment following the procedure described in Section 2.2 and discuss the obtained results in detail.

Firstly, we want to look into the mean probabilities $\langle \mathbb{P} \rangle$ for ALPs to decay within our different detector volumes. In Figure 3.5 these are depicted in dependence of the coupling $c_l/\Lambda$. Each plot for all detectors respectively contains all considered mass scenarios.

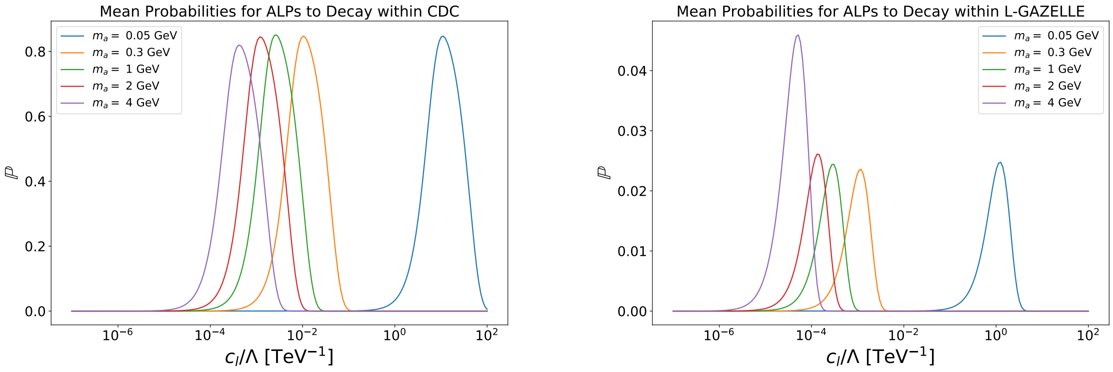

**(a)** CDC **(b)** L-GAZELLE

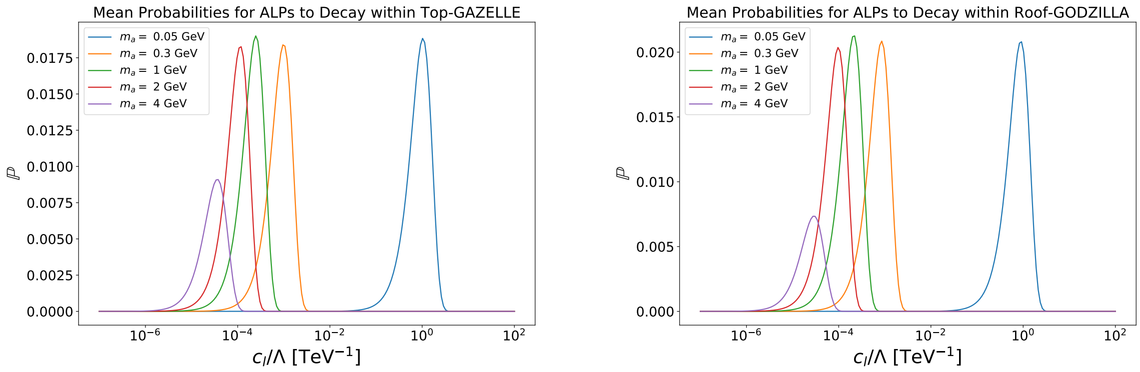

**(c)** Top-GAZELLE **(d)** Roof-GODZILLA

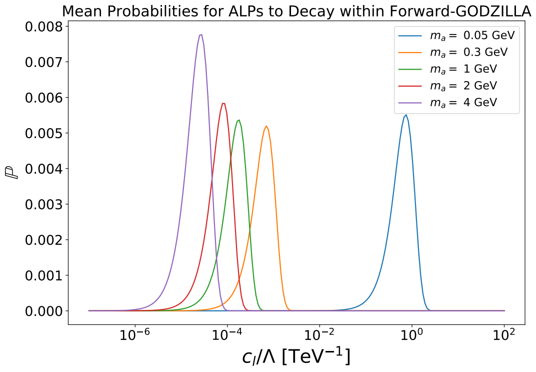

**(e)** Forward-GODZILLA

**Figure 3.5:** Mean decay probabilities for single detectors

For all detectors, the plots have the same general structure: one finds one peak in the probabilities for each ALP mass, where the position of the peak, i.e. the corresponding coupling $c_l/\Lambda$, grows with decreasing mass. This behaviour is completely as expected as the lifetime increases with decreasing mass and reduces with growing coupling (Equation 2.4) and thus a bigger coupling is needed for lighter ALPs to get the same lifetime.
However, the 0.05 GeV peak is significantly more shifted to bigger couplings than the others. This is due to the fact that the 0.05 GeV ALP is the only ALP which is too light to decay into muons. This increases its lifetime by orders of magnitude and therefore these significantly bigger couplings are needed to get the same lifetime as the heavier ALPs.

Of course, the plots for the different detectors also differ in many aspects. Firstly and foremost, the relative heights of the different mass peaks within one detector's plot vary. While the 4 GeV peak is clearly smaller than the others for Top-GAZELLE and Roof-GODZILLA, the complete opposite is the case for L-GAZELLE and Forward-GODZILLA. This can be easily understood by recalling that the 4 GeV ALP is much more likely to have a forward boost while the lighter ALPs are produced more in transverse direction (see Section 3.3 and Figure 3.4c). Therefore, Top-GAZELLE and Roof-GODZILLA, which are positioned in transverse direction, cover the lighter ALPs much better than the 4 GeV ALP and L-GAZELLE and Forward-GODZILLA, which have a better forward coverage, are more sensitive to the heavy ALP. For the CDC, all peaks are of equal height due to its outstanding solid angle coverage and the thus resulting good coverage of all scenarios.
Another obvious difference is the absolute heights of the peaks for the different detectors. Here, the CDC performs by far best with maximum decay probabilities of $\langle\mathbb{P}\rangle^{\max} \gtrsim 0.8$, followed by L-GAZELLE, Roof-GODZILLA, Top-GAZELLE and lastly Forward-GODZILLA. The maximum decay probabilities $\langle\mathbb{P}\rangle^{\max}$ are mostly affected by the distance of the detector to the interaction point (exponential decay law; see Equation 2.7) and the solid angle coverage. The mean radial thickness also has an effect on $\langle\mathbb{P}\rangle^{\max}$, but is rather minor compared to the two aspects before. Given that the CDC has the closest distance to the interaction point and (by far) the best angular coverage, the high decay probabilities are completely as expected.
Moreover, the position of a peak with given ALP mass differs for the different detectors. The farther the detector is away from the interaction point, the more the peaks are located at lower $c_l/\Lambda$, because the farther the distance, the longer the lifetime of the ALP needs to be to arrive at the detector and thus smaller couplings are needed.
This difference in peak positions can best be seen when plotting the mean probabilities for one specific mass but all detectors in one graph. This is done in Figure 3.6 for $m_a = 0.3\,\text{GeV}$ and $m_a = 4\,\text{GeV}$ (the 0.3 GeV ALP represents all the other light scenarios because all plots look qualitatively equal for them).

More importantly, in these plots the one most relevant thing can be seen: whether there are regions in $c_l/\Lambda$, where the mean decay probability $\langle\mathbb{P}\rangle$ is higher for any of the far detectors than it is for the CDC, because only then, a gain in sensitivity over the existing Belle II detector can be achieved.

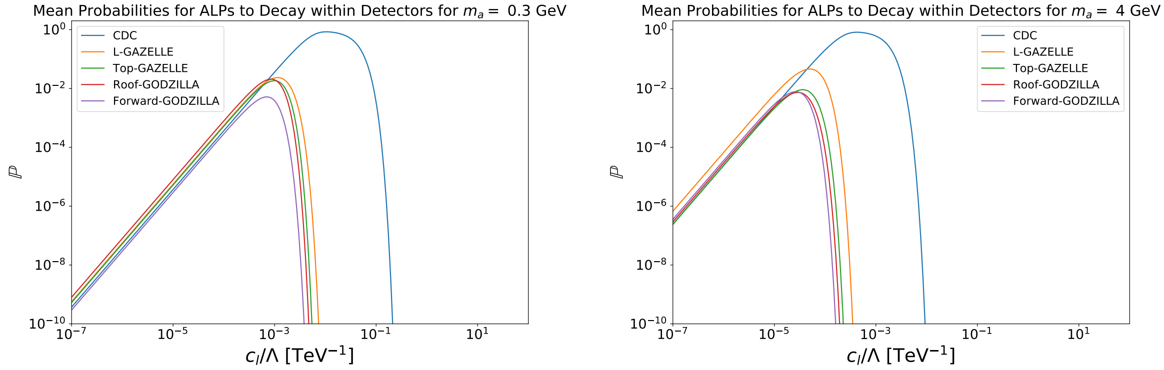

**(a)** $m_a = 0.3\,\mathrm{GeV}$ **(b)** $m_a = 4\,\mathrm{GeV}$

**Figure 3.6:** Mean decay probabilities for single masses

For the 0.3 GeV ALP (and thus for all light ALPs), we see higher mean probabilities over the CDC for L-GAZELLE, Top-GAZELLE and Roof-GODZILLA in the region $c_l/ \lesssim 10^{-3}\,\mathrm{TeV}^{-1}$. Here, Roof-GODZILLA provides the highest probabilities and thus the gain in sensitivity of Roof-GODZILLA is expected to be best for the light ALP scenarios. For the 4 GeV ALP on the other hand, only L-GAZELLE exceeds the CDC significantly in the range $c_l/ \lesssim 10^{-4}\,\mathrm{TeV}^{-1}$ and Forward-GODZILLA exceeds the CDC slightly in the range $c_l/ \lesssim 10^{-5}\,\mathrm{TeV}^{-1}$. Top-GAZELLE and Roof-GODZILLA approximately coincide with the CDC in this region. Thus the gain in sensitivity of L-GAZELLE is expected to be best for the heavy ALP scenario.
Again, our expectations turn out to be true: Roof-GODZILLA and Top-GAZELLE cover the transverse direction and thus exceed CDC's performance for the light scenarios, Forward-GODZILLA covers the forward direction and thus exceeds (though only slightly) CDC's performance for the heavy scenario and L-GAZELLE is an allrounder which offers gains for all scenarios.

The next step in the analysis is the calculation of the mean number $N_{dec}$ of expected detected ALPs in the detectors. We proceed exactly as described in Section 2.2 to determine $N_{dec}$ as a function of $c_l/\Lambda$ for the Belle II GAZELLEs. In Figure 3.7, we plot $N_{dec}$ for one specific mass and all detectors in one graph. This is done for the 0.3 GeV ALP, which again represents all the other light ALPs, and the 4 GeV ALP. The horizontal line in both plots marks $N_{dec} = 3$ and therefore the intersections of the plots with this line gives the bounds of sensitivity for the detectors (recall, that the region with $N_{dec} \geq 3$ is the sensitive region for a detector; see Section 2.2).

One immediately sees that the shape of these plots looks very similar to the mean probability plots in Figure 3.6. This however is not surprising at all because to obtain $N_{dec}(c_l/\Lambda)$, $\langle\mathbb{P}\rangle(c_l/\Lambda)$ is simply multiplied by a factor which is equal for all graphs in one plot as the corresponding mass is identical (see Equation 2.11).
For the 0.3 GeV ALP, the detectors Roof-GODZILLA, L-GAZELLE and Top-GAZELLE have smaller lower sensitivity bounds in $c_l/\Lambda$ and thus, these three detectors exceed

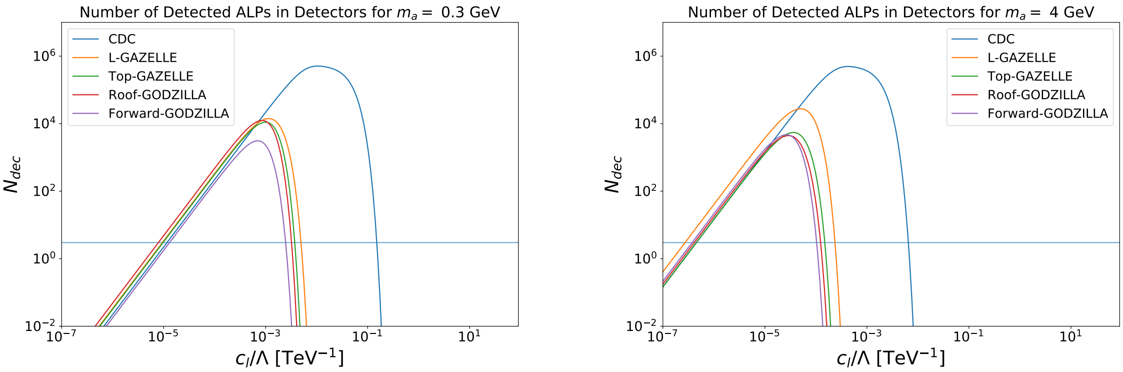

**(a)** $m_a = 0.3\,\mathrm{GeV}$ **(b)** $m_a = 4\,\mathrm{GeV}$

**Figure 3.7:** Mean number of expected detected ALPs for single masses

CDC's sensitivity for the discovery of the light ALPs. Roof-GODZILLA has the smallest lower bound and therefore offers the biggest gain in sensitivity. Interestingly, L-GAZELLE performs slightly better than Top-GAZELLE although Top-GAZELLE was specifically designed to cover the transverse direction, i.e. the light ALPs, and L-GAZELLE was "only" designed as an allrounder. Forward-GODZILLA offers no gain in sensitivity for the light ALP, which is completely as expected as it solely covers the forward direction, i.e. the heavy ALP.
For the 4 GeV ALP, the detectors L-GAZELLE and Forward-GODZILLA have smaller sensitivity bounds in $c_l/\Lambda$ than the CDC and thus exceed CDC's performance for the heavy ALP. The detectors Roof-GODZILLA and Top-GAZELLE both coincide with the CDC in the bounds and thus do not offer any gain in sensitivity here. L-GAZELLE has by far the best performance for the 4 GeV ALP and therefore again outperforms a detector which has been specifically designed to cover this scenario (Forward-GODZILLA).

To quantify the regions of sensitivity and the corresponding gain over the CDC, we can extract the numeric values for the lower bounds in $c_l/\Lambda$ for all detectors and mass scenarios as the intersection of the plots in Figure 3.7 with the $N_{dec} = 3$-line. In Table 3.2, these lower bounds are summarized.
However, to have the direct comparison to the CDC, we determine the ratio in lower bounds $(c_l/\Lambda)^{\mathrm{GAZELLE}}_{\mathrm{min}}/(c_l/\Lambda)^{\mathrm{CDC}}_{\mathrm{min}}$. So a value smaller than one indicates a gain in sensitivity over the CDC for the detection of ALPs. These results are enlisted in Table 3.3.

|  | CDC | LG | TG | RG | FG |
|---|---|---|---|---|---|
| 0.05 GeV | $1.22 \times 10^{-2}$ | $9.83 \times 10^{-3}$ | $1.00 \times 10^{-2}$ | $8.21 \times 10^{-3}$ | $1.32 \times 10^{-2}$ |
| 0.3 GeV | $1.16 \times 10^{-5}$ | $9.41 \times 10^{-6}$ | $9.71 \times 10^{-6}$ | $7.88 \times 10^{-6}$ | $1.30 \times 10^{-5}$ |
| 1 GeV | $2.91 \times 10^{-6}$ | $2.35 \times 10^{-6}$ | $2.39 \times 10^{-6}$ | $1.94 \times 10^{-6}$ | $3.19 \times 10^{-6}$ |
| 2 GeV | $1.36 \times 10^{-6}$ | $1.08 \times 10^{-6}$ | $1.12 \times 10^{-6}$ | $9.13 \times 10^{-7}$ | $1.45 \times 10^{-6}$ |
| 4 GeV | $4.51 \times 10^{-7}$ | $2.72 \times 10^{-7}$ | $4.55 \times 10^{-7}$ | $4.11 \times 10^{-7}$ | $3.73 \times 10^{-7}$ |

**Table 3.2:** Lower bounds of sensitivity $(c_l/\Lambda)_{\min}$ [TeV$^{-1}$]

|  | CDC | LG | TG | RG | FG |
|---|---|---|---|---|---|
| 0.05 GeV | 1 | 0.81 | 0.82 | 0.67 | 1.09 |
| 0.3 GeV | 1 | 0.81 | 0.84 | 0.68 | 1.12 |
| 1 GeV | 1 | 0.81 | 0.82 | 0.67 | 1.10 |
| 2 GeV | 1 | 0.79 | 0.82 | 0.67 | 1.07 |
| 4 GeV | 1 | 0.60 | 1.01 | 0.91 | 0.83 |

**Table 3.3:** Fraction of lower bounds of sensitivity $(c_l/\Lambda)_{\min}^{\text{GAZELLE}}/(c_l/\Lambda)_{\min}^{\text{CDC}}$

Firstly, one nicely sees the equal behaviour of all the light ALPs, i.e. $m_a \leq 2\,\text{GeV}$, in the fractions of the lower bounds in Table 3.3: they are essentially identical for one respective detector for all the light ALPs. Moreover, these numeric results confirm what we have already seen throughout the entire analysis; Roof-GODZILLA offers the biggest gain in sensitivity for the light ALPs and L-GAZELLE offers the biggest gain in sensitivity for the heavy ALP. However, L-GAZELLE also performs well for the light ALPs (even better than Top-GAZELLE). This shows that the design of L-GAZELLE, i.e. position, size and shape, is the optimal choice to cover all mass scenarios.

However, none of the far detectors under study gives an improvement in sensitivity over the Belle II main detector by orders of magnitude; not even an improvement by a factor of 2 is achieved. This is simply due to the exceptionally good angular coverage and size of the CDC (see Section 3.1) and the thus already exceptionally good sensitivity for the discovery of ALPs over a wide range in parameter-space. Hence, it is questionable, whether the small gains of a far detector at Belle II would be worth the expenses and constructional efforts to build such a far detector. This result can be considered very positive because it implies that Belle II's main detector already is sensitive to the detection of long-lived particles and no expensive far detectors need to be constructed.

# 4 ILC

## 4.1 Detectors

In this section, we discuss firstly the experimental setup at the International Linear Collider (ILC) and secondly the detector geometries which are going to be investigated.

The labframe's coordinate system is from here on defined as follows: the center $(0,0,0)$ coincides with the collision point of electron and positron, the $z$-axis coincides with the electron-beam, the $y$-axis points vertically upwards and the $x$-axis is then determined by the other two axes. In this frame, spherical coordinates $(r,\theta,\phi)$ and cylindrical coordinates $(\rho,\phi,z)$ are defined as usual.

### 4.1.1 The International Linear Collider

The International Linear Collider is a proposed linear electron-positron collider, planned to be built in Japan. It is designed to operate at center of mass energies continuously adjustable in the range $[200\,\mathrm{GeV}, 500\,\mathrm{GeV}]$ with an option to upgrade to $1\,\mathrm{TeV}$ [24, 25].

Depending on the energy used, different physics can be investigated; e.g. at $\sqrt{s} = 250\,\mathrm{GeV}$, the dominant process under study will be $e^+e^- \to Zh$ and the associated physics aim is the precise measurement of the Higgs couplings, whereas at $\sqrt{s} = 500\,\mathrm{GeV}$, the dominant process under study will be $e^+e^- \to Zhh$ or $e^+e^- \to ht\bar{t}$ and the associated physics aim is the precise measurement of the Higgs selfcouplings and Higgs-top couplings [24, 17]. In general, the aim of the ILC will be the precise measurement of the Higgs mass and couplings as well as the top mass and moreover the search for new physics beyond the Standard Model.

The in total $\sim 31\,\mathrm{km}$ long linear collider (see Figure 4.1) will operate at a high luminosity of $L = 0.75 \times 10^{34}\,\mathrm{cm}^{-2}\mathrm{s}^{-1}$ and aims at collecting an integrated luminosity of $\int L\mathrm{d}t = 250\,\mathrm{fb}^{-1}$ for $\sqrt{s} = 250\,\mathrm{GeV}$ [17, 24, 25]. This high luminosity together with the clean environment of non-hadronic collisions will allow for ultra-precision measurements of the Higgs boson, exceeding the precision of the LHC [24].

In contrast to SuperKEKB, the ILC is linear and not circular. This opens the possibility of using polarized electrons and positrons because polarization is preserved in linear colliders during acceleration. By preparing the electrons in a 80% left-handed state and the positrons in a 30% right-handed-state, the luminosity can be increased by a factor of up to $\sim 2$ realtive to non-polarized beams [26].

Another contrast to SuperKEKB is the energy symmetry of electron and positron, i.e. the center of mass is not boosted for the ILC. This of course leads to different kinematics than in Belle II.

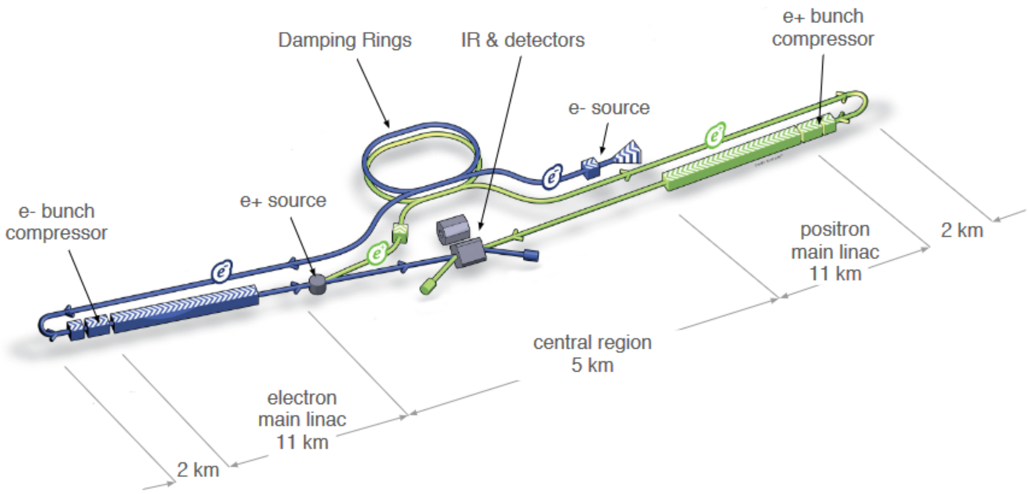

**Figure 4.1:** Schematic of the ILC; taken from [24]

The ILC will have two different detectors, the International Large Detector (ILD) and the SiD, to carry out experiments. They are designed to share the same interaction point and can be exchanged by a simple push-pull system [24, 26].
Both detectors can perform high-precision measurements and serve multiple purposes. However, the ILD is larger and thus better suited for our ALP-search. Therefore, we will focus our analysis entirely on the ILD.

The ILD consists of several subdetectors which are cylindrically arranged around the beam (see Figure 4.2). Closest to the interaction point, a multi-layer pixel vertex detector (VTX) reconstructs vertices with high precision. The Time Projection Chamber (TPC) serves the purpose of continuous tracking together with timestamps along each track. Furthermore, energy loss, which is crucial for particle identification, as well as momenta can be measured within TPC. A highly segmented electromagnetic and hadronic calorimeter (ECAL and HCAL) measure energies and provide spatial information with nearly full angular coverage. Lastly, an iron yoke controls the magnetic flux in the detector and simultaneously serves as muon detector [26].

As for the GAZELLE analysis in the Belle II part, we will compare the GAZELLEs' performances with the tracking detectors of ILD, i.e. the TPC and the VTX. We assume perfect detection efficiency within the detector volume, given by $z \in [-235\,\text{cm}, 235\,\text{cm}]$, $\theta \in [8^\circ, 172^\circ]$ and $\rho \geq 0.6\,\text{cm}$. This ILD design has a solid angle of $\Omega = 12.55$ (99% angular coverage) and a mean radial thickness of $D = 2.18\,\text{m}$.

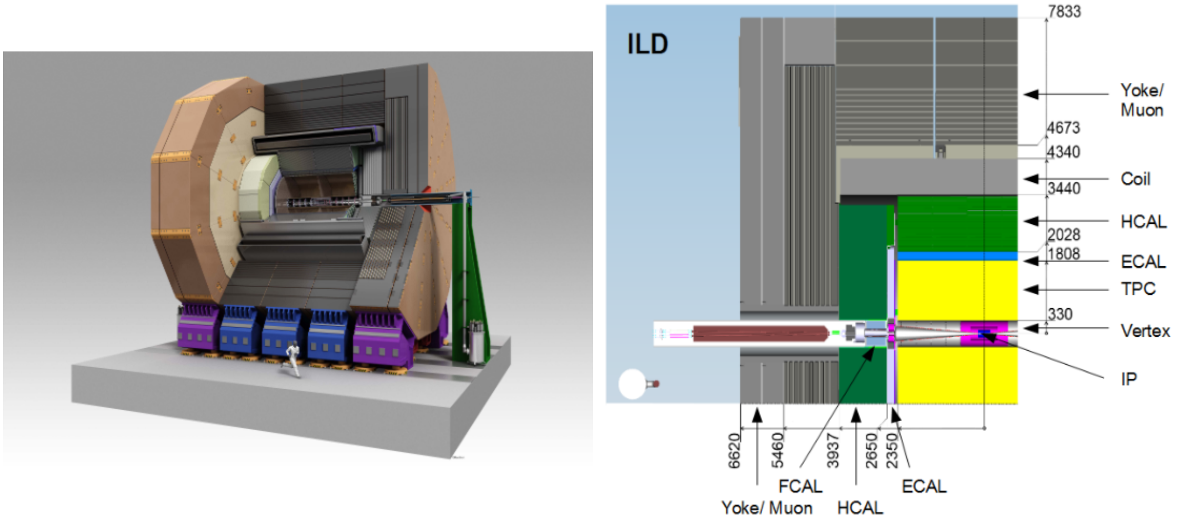

**Figure 4.2:** Schematics of the ILD (lengths in mm); taken from [26]

### 4.1.2 GAZELLE Detectors at ILC

The general technical requirements for the GAZELLE detectors at ILC are essentially the same as for Belle II and are therefore already described in Section 3.1.2. One difference however is the need for higher spatial resolution in tracking due to the much larger boost of particles at the ILC compared to Belle II and the thus smaller opening angle between the two lepton-tracks of an ALP decay. As before, we assume 100% detection efficiency within the detector volume.

In the ILC analysis, we study three different far-detector geometries: Vertical-Shaft-GAZELLE (VS), Side-Shaft-GAZELLE (SS) and Huge-GODZILLA (HG). Just as in the Belle II part, their performances will be analyzed and compared to the ILC main detector, the ILD as described above (see Section 4.1.1), to assess possible gains in sensitivity for ALP-decays.
It must be noted that the ILC detector hall is 70 m underground (in contrast to Tsukuba Hall at Belle II, which is approximately on ground level). Thus, two of the GAZELLEs, VS-GAZELLE and SS-GAZELLE, are placed in tunnels around the detector hall.

- **Vertical-Shaft-GAZELLE:**
  Vertical-Shaft-GAZELLE is a $(18 \times 30 \times 18)$m cuboid centered around $(0, 45, 0)$m. It is placed in the vertical tunnel directly above the interaction point, which is used for lowering the ILD and SiD into the detector hall. This detector will therefore solely detect particles which are emitted in transverse direction. VS-GAZELLE has a solid angle of $\Omega = 0.33$ (2.6% angular coverage) and a mean radial thickness of $D = 15.8\,\text{m}$.

- **Side-Shaft-GAZELLE:**
  Side-Shaft-GAZELLE is a $(140 \times 10 \times 10)$m cuboid centered around $(0, -5, -35)$m. It is placed in the horizontal access tunnel going parallel to the detector hall, right underneath the electron beam. This detector will therefore mostly detect particles which are emitted in longitudinal direction. SS-GAZELLE has a solid angle of $\Omega = 0.58$ (4.6% angular coverage) and a mean radial thickness of $D = 10.6\,\text{m}$.

- **Huge-GODZILLA:**
  Huge-GODZILLA is a $(1000 \times 10 \times 1000)$m cuboid centered around $(0, 75, 0)$m. It is placed on ground level above the interaction point. This detector will therefore mostly detect particles which are emitted in transverse direction, but also the forward direction is covered well due to HG's enormous size. HG has a solid angle of $\Omega = 5.49$ (43.7% angular coverage) and a mean radial thickness of $D = 23.0\,\text{m}$. Of course, a $1\,\text{km}^2$-detector is a not very realistic design, but it will be interesting to see, whether the enormous size can compensate for the far distance between detector and interaction point.

To visualize the different geometries under study, schematics of the side- and topview of all detectors are given in Figure 4.3.

As we see in Equation 2.10, the quantity $D \times \Omega$ gives first insight into a detector's sensitivity in the long decaylength limit. Thus, these values are gathered in Table 4.1.

| | ILD | VS | SS | HG |
|---|---|---|---|---|
| $\Omega$ | 12.55 | 0.33 | 0.58 | 5.49 |
| $D$ [m] | 2.18 | 15.8 | 10.6 | 23.0 |
| $\Omega \times D$ [m] | 27.3 | 5.2 | 6.1 | 126.3 |

**Table 4.1:** Solid angle, mean radial thickness and their product for all detectors

## 4.2 Backgrounds

Just like for the Belle II GAZELLEs, any event which contains two charged particles in the final state is a possible background. In principle, all the different sources of backgrounds as discussed in the Belle II part (see Section 3.2) are still valid background events at the ILC and they can be rejected by the same means as before.
Due to the much greater center of mass energy, new events, which have not been kinematically possible at Belle II, like e.g. $Z \to f\overline{f}$, $h \to f\overline{f}$ or $h \to W^+W^-$ pose further possible types of backgrounds. Nevertheless, all these examples are very unlikely to be significant sources of backgrounds in far-detectors because the Z-boson as well as the Higgs will certainly decay within the ILD and not reach any GAZELLE detector.

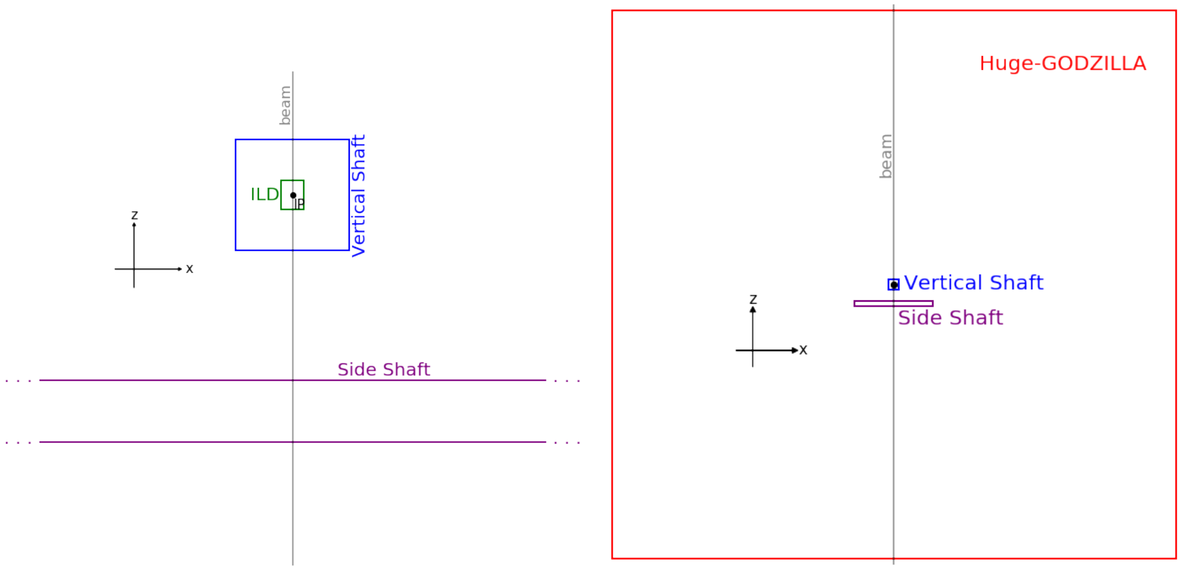

**(a)** Topview without HG **(b)** Topview

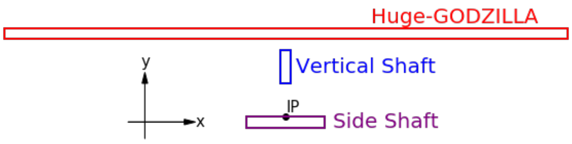

**(c)** Sideview

**Figure 4.3:** Schematics of all detectors at ILC

It must be stressed that no detailed backgrounds study has been conducted for ILC far detectors and thus we can only assume that the situation is similar to Belle II backgrounds. However, just like for Belle II it seems reasonable that all backgrounds can be rejected effectively and therefore the following work will again be carried out with a zero-background assumption.

## 4.3 Kinematic Distributions

In this section, we want to examine the kinematic distributions of the ALPs in the different production processes at the ILC (see Section 2.1). This will help us to understand the results of the detector-analysis below and it played a crucial role in the exact design and positioning of the GAZELLEs under study.
Just as in the Belle II part, the distributions of interest are the $\theta$-, $p_T$ and $E$-distribution.

It must be emphasized that these quantities refer to the ALP and not to any of the other particles in the respective final states of the different production processes.

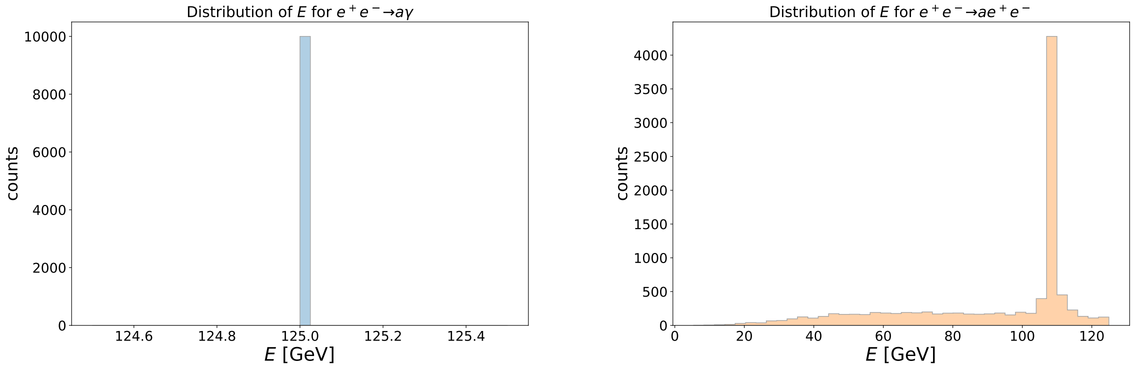

**(a)** $E$-distribution of $e^+e^- \to a\gamma$

**(b)** $E$-distribution of $e^+e^- \to ae^+e^-$

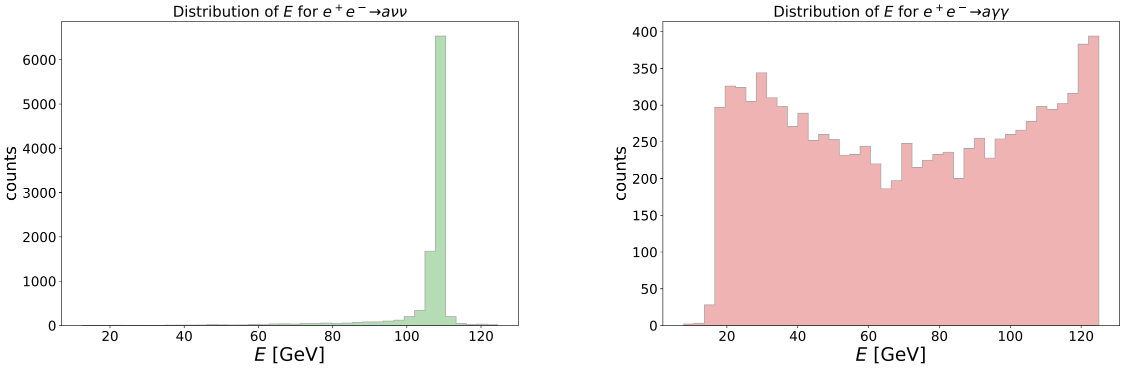

**(c)** $E$-distribution of $e^+e^- \to a\nu\nu$

**(d)** $E$-distribution of $e^+e^- \to a\gamma\gamma$

**Figure 4.4:** $E$-distributions of the ALPs at ILC

### 4.3.1 $E$-Distributions

The energy distributions for all production channels are depicted in Figure 4.4.
For the channel $e^+e^- \to a\gamma$, we see a very simple structure: all ALPs have an energy of $E \approx 125\,\text{GeV} = \sqrt{s}/2$; i.e. photon and ALP evenly share the entire cm-energy. This is a characteristic behaviour for an s-channel process with two final state particles with negligible mass (one really being massless) compared to the total energy.
The distributions of $e^+e^- \to ae^+e^-$ and $e^+e^- \to a\nu\nu$ have a similar structure. Both are strongly peaked at $E \approx 110\,\text{GeV} < \sqrt{s}/2$ with only very few events with energy above or below. One can understand this with the following (very qualitative) interpretation of the respective Feynman diagrams (see Figure 2.2b, 2.2c): the initial electron and positron radiate off a Z-boson (W-boson) which carries away half of their initial energy,

leaving the final state electron and positron (neutrinos) with an energy of $E_{e/\nu} \approx \sqrt{s}/4$. The ALP is created by the fusion of the two bosons which together give an energy of $E \approx \sqrt{s}/2$; thus the strong peak in the energy distributions. The shift of the peak to a lower energy of $E \approx 110\,\text{GeV}$ is the result of the three-body phase space. In the case of $e^+e^- \to a\nu\nu$, nearly all events are contained in the peak while for $e^+e^- \to ae^+e^-$, very few ALPs have energies below and above the peak. This difference occurs because of the different masses of electron and neutrino which affects the final state phase space.
The energy distribution of the channel $e^+e^- \to Z\gamma \to a\gamma\gamma$ differs significantly from the others. Here, one can not find one clear peak; we rather have a much more uniform distribution between 20 GeV and 125 GeV with slight peaks to both ends of the distribution. This drastic difference is due to the Z-boson being created on-shell in this process and not as an off-shell particle like in the other processes. Apparently, the ALPs in this channel have a smaller energy on average and thus a smaller boost. This then leads to smaller decaylengths (in the labframe) at equal couplings which we will see later again in the analysis.

### 4.3.2 $p_T$-Distributions

The transverse momentum distributions are depicted in Figure 4.5a for all four production channels. The first observation applying for all channels is the general shape of the distributions: a gradual rise to a peak at some $p_T$ and a strong decrease after the peak. The differences obviously are the positions of the peaks and the form of the rise before the peaks.
For $e^+e^- \to a\gamma$, the distribution is strongly peaked at $p_T \approx 125\,\text{GeV}$ with most events in this high-momentum region. This is simply due to the fact that most of the ALP's energy is contained in transverse momentum and the strong peak of the energy distribution at 125 GeV (see Figure 4.4a).
The distributions for $e^+e^- \to ae^+e^-$ and $e^+e^- \to a\nu\nu$ are both peaked at $p_T \approx 110\,\text{GeV}$. The explanation is just as before: most of the ALP's energy, which peaks at 110 GeV (see Figure 4.4b,4.4c), is contained in transverse momentum. The peaks are not as strong as for the channel $e^+e^- \to a\gamma$ because already the peaks in the $E$-distributions are weaker.
Finally, the $p_T$-distribution for the channel $e^+e^- \to Z\gamma \to a\gamma\gamma$ differs significantly again. Here, we have a peak at $p_T \approx 45\,\text{GeV} \approx m_Z/2$ with a much steeper rise before the peak than in the other channels. In the first part of the process, i.e. $e^+e^- \to Z\gamma$, the Z-boson obtains a strong boost in forward or backward direction. When the Z then decays into the ALP and the photon, the longitudinal momentum from the forward/backward boost must be conserved and thus, transverse momentum can only originate from the Z-mass. This transverse momentum is evenly shared by ALP and photon which explains the peak in $p_T$ at $m_Z/2$ and the steep fall afterwards. Of course, not all of the Z-mass must be converted in transverse momentum which is why there are also many events below the peak.

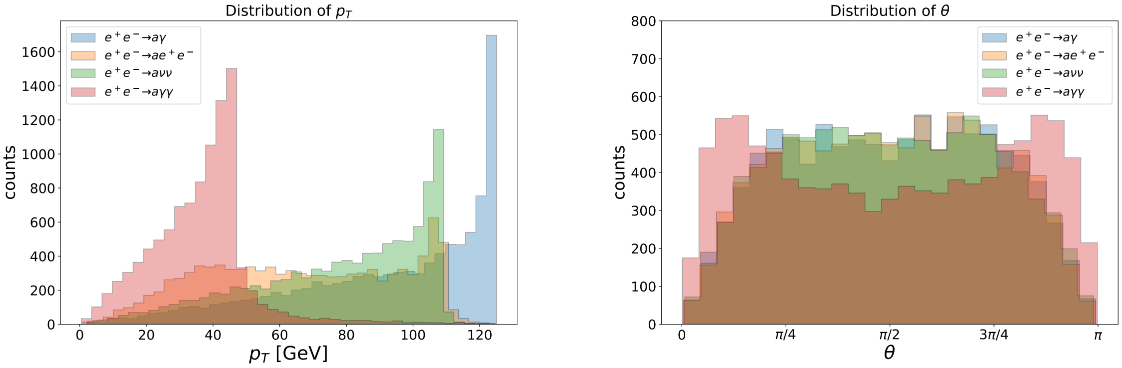

**(a)** $p_T$-distribution

**(b)** $\theta$-distribution

**Figure 4.5:** $p_T$- and $\theta$-distribution of ALPs at ILC

### 4.3.3 $\theta$-Distributions

The $\theta$-distributions for all channels are depicted in Figure 4.5b.
One clearly sees that the $\theta$-distributions for the channels $e^+e^- \to a\gamma$, $e^+e^- \to ae^+e^-$ and $e^+e^- \to a\nu\nu$ look very alike. All three distributions seem relatively uniform in the range $\frac{\pi}{4} \leq \theta \leq \frac{3\pi}{4}$ and then fall off to the edges, i.e. forward and backward direction. We have already concluded before that most of the ALP's energy is contained in the transverse momentum for the three channels under discussion. Therefore, it makes perfect sense that the $\theta$-distributions are maximum around $\theta = \frac{\pi}{2}$, i.e. transverse direction and then decrease in forward and backward direction.
The $\theta$-distribution for the channel $e^+e^- \to Z\gamma \to a\gamma\gamma$ however looks entirely different. Here, one sees two clear peaks in forward and backward direction and fewer events in the transverse region. Again, we employ an argument from before to explain this behaviour. The Z-boson, which decays into ALP and photon, is strongly boosted in forward or backward direction. The ALP inherits this boost and obtains less transverse momentum than in the other channels and therefore is emitted in forward or backward direction.
This general difference in directions of emission between the three channels $e^+e^- \to a\gamma$, $e^+e^- \to ae^+e^-$, $e^+e^- \to a\nu\nu$ and $e^+e^- \to Z\gamma \to a\gamma\gamma$ on the other side will later be visible very clearly in the detector analysis.

## 4.4 Analysis

In this section, we carry out the detector analysis for the ILC, exactly following the procedure described in Section 2.2, and discuss the obtained results in detail.

Firstly and exactly like in the Belle II part, we want to examine the mean probabilities $\langle\mathbb{P}\rangle$ for ALPs to decay in the different detectors under study, which is, due to the assumed

100% detection efficiency and zero backgrounds, identical to the mean probability for an ALP to be detected by the given detector. In Figure 4.6, $\langle \mathbb{P} \rangle$ is plotted as a function of the coupling $c_l/\Lambda$. Each plot for all single detectors respectively contains all four production channels.

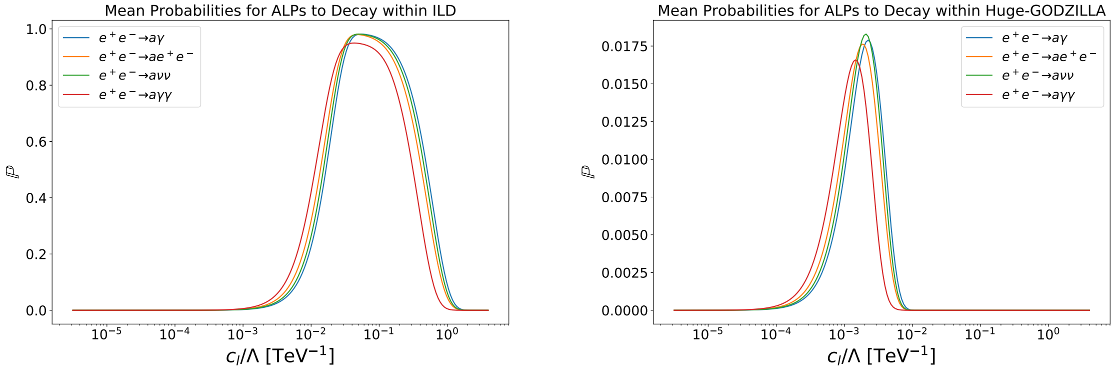

**(a)** ILD **(b)** Huge-GODZILLA

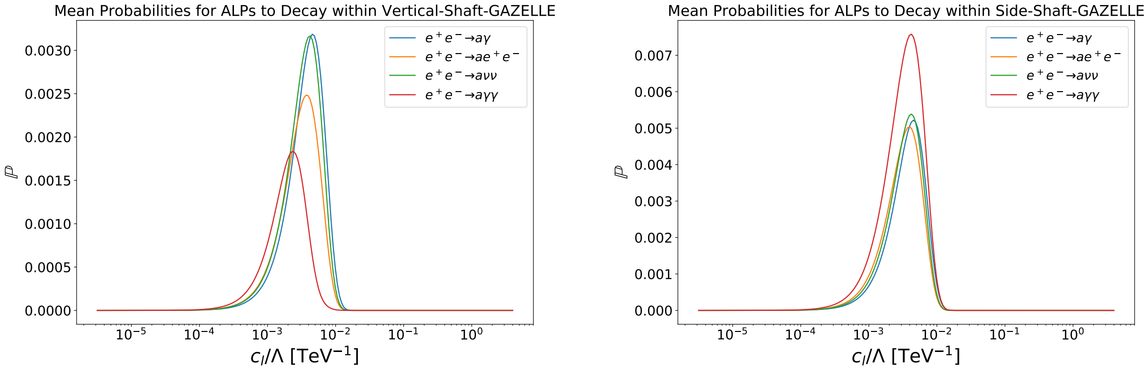

**(c)** Vertical-Shaft-GAZELLE **(d)** Side-Shaft-GAZELLE

**Figure 4.6:** Mean decay probabilities for single detectors

All plots have the same general structure: for each production channel, one finds one clear peak in the probabilities where the position of the peaks, i.e. the corresponding coupling $c_l/\Lambda$, is nearly identical for the four different channels for one given detector. Solely the peak of the channel $e^+e^- \to Z\gamma \to a\gamma\gamma$ deviates and is shifted to slightly smaller couplings. This can be understood by remembering that the average boost of the ALPs in this channel is smaller than for the other channels (see Section 4.3, Figure 4.4) and therefore smaller couplings are needed to obtain the same decay-length (in the labframe).

Of course, there are many aspects where the mean probabilities for the different detectors differ.
Firstly, the relative heights of the peaks for the different channels vary. While all peaks are approximately of equal height for the ILD and Huge-GODZILLA, the $(e^+e^- \to$

$Z\gamma \to a\gamma\gamma$)-peak is about half as high as the other peaks for Vertical-Shaft-GAZELLE (though the ($e^+e^- \to ae^+e^-$)-peak also deviates here and its height is in between the ($e^+e^- \to Z\gamma \to a\gamma\gamma$)-peak and the remaining two peaks) and about 1.5 times as high as the other peaks for Side-Shaft-GAZELLE. As we have seen in Section 4.3, ALPs from $e^+e^- \to Z\gamma \to a\gamma\gamma$ are emitted preferably in forward/backward direction while ALPs from the other channels are located more in transverse direction. All peaks are of equal height for ILD and Huge-GODZILLA because both detectors have good angular coverages (see Section 4.1) and therefore detect ALPs in transverse as well as in forward/backward direction. Side-Shaft-GAZELLE on the other hand covers the forward/backward direction much better than the transverse direction. Thus, ALPs from $e^+e^- \to Z\gamma \to a\gamma\gamma$ have a higher probability to be detected. The exact opposite is the case for Vertical-Shaft-GAZELLE which solely covers the transverse direction. The slightly reduced probability for the ($e^+e^- \to ae^+e^-$)-peak here arises from the fact that Vertical-Shaft-GAZELLE covers only a small solid angle in the transverse direction (see Figure 4.1, Table 4.1) and that the ALPs from $e^+e^- \to ae^+e^-$ are (very) slightly less transverse than ALPs from $e^+e^- \to a\gamma$ and $e^+e^- \to a\nu\nu$ (see the $p_T$-distributions; Figure 4.5a).

Secondly, the absolute heights $\langle \mathbb{P} \rangle^{\max}$ of the peaks differ for the different detectors. Here, the ILD performs by far best with maximum probabilities of $\langle \mathbb{P} \rangle^{\max} \approx 1$, followed by Huge-GODZILLA, Side-Shaft-GAZELLE and lastly Vertical-Shaft-GAZELLE. As already discussed in the Belle II part (see Section 3.4), the maximum decay probabilities $\langle \mathbb{P} \rangle^{\max}$ are mostly affected by the distance of the detector to the interaction point (exponential decay law; see Equation 2.7) and the solid angle coverage. The mean radial thickness also has an effect on $\langle \mathbb{P} \rangle^{\max}$, but it is rather minor compared to the two aspects before. Given that the ILD is closest to the interaction point and has (by far) the best angular coverage (see Section 4.1), it is not surprising that it performs best here. Although Huge-GODZILLA has the largest distance to the interaction point, its maximum decay probabilities are better than Vertical-Shaft- and Side-Shaft-GAZELLE. Its far better angular coverage (see Table 4.1) outweighs the longer distance to the interaction point.

Thirdly, one clearly sees that the probability-peaks for the ILD are wider in $c_l/\Lambda$ than for the other detectors. This is due to the very close distance of the ILD to the interaction point: the exponential decay law (see Equation 2.7) results in a constant unit of detector thickness $\Delta D$ covering a wider range of decay-length $\Delta c\tau$, which is equivalent to a wider range of coupling $\Delta(c_l/\Lambda)$, if it is closer to the interaction point. Therefore, the ILD covers a far wider range in $c_l/\Lambda$ than the other detectors despite having a mean radial thickness $D$ which is up to $\sim 10$ times smaller (see Table 4.1). Interestingly, this effect is not as striking for the CDC of Belle II (see Figure 3.5). The 0.3 cm that the ILD is closer to the interaction point than the CDC really must make such a great difference. So here, one sees that every millimeter distance of an experiment's main detector to the interaction point can have effects on the performance of that detector.

Lastly, the positions of the peaks in $c_l/\Lambda$ differ for the different detectors. The reason is exactly the same as in the Belle II part: The farther the detector is away from the interaction point, the more the peaks are located at lower $c_l/\Lambda$, because the farther the distance, the longer the lifetime of the ALP needs to be to arrive at the detector and thus smaller couplings are needed. This can be seen especially well for Huge-GODZILLA (see Figure 4.6b).

This difference in peak positions can best be seen when plotting the mean decay probabilities for all the different detectors for the single channels respectively in one graph. This is done in Figure 4.7 only for the channels $e^+e^- \to a\gamma$ and $e^+e^- \to Z\gamma \to a\gamma\gamma$ because the results look qualitatively identical for the remaining two channels.

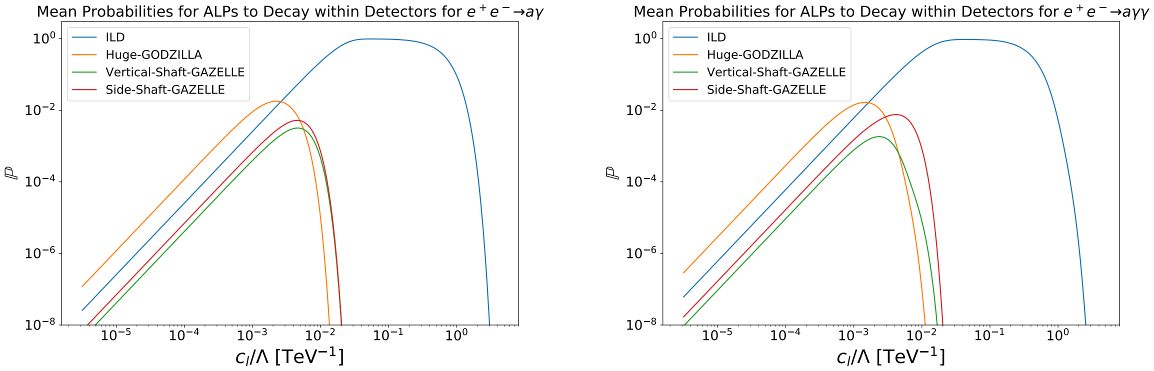

**(a)** $e^+e^- \to a\gamma$

**(b)** $e^+e^- \to Z\gamma \to a\gamma\gamma$

**Figure 4.7:** Mean decay probabilities for single channels

One can see one much more important aspect in these plots: whether there are regions in $c_l/\Lambda$, where the mean probabilities for ALPs to be detected is higher for one of the far-detectors than for the ILD. Because only then and only in this region a gain in sensitivity over the ILD can be expected. In all channels, merely Huge-GODZILLA achieves this for $c_l/\Lambda \lesssim 10^{-3}\,\text{TeV}^{-1}$, while Vertical-Shaft- and Side-Shaft-GAZELLE yield smaller probabilities than the ILD for all couplings. So already at this point, we can conclude that the only promising far detector under study is Huge-GODZILLA.

The next step in the analysis is the calculation of the mean number $N_{dec}$ of expected detected ALPs in the detectors. We proceed exactly as described in Section 2.2 to firstly calculate $N_{dec}$ as a function of the coupling $c_l/\Lambda$. In Figure 4.8a, $N_{dec}(c_l/\Lambda)$ is depicted for all detectors but only for the channels $e^+e^- \to a\gamma$ and $e^+e^- \to Z\gamma \to a\gamma\gamma$ because the results look qualitatively identical for the remaining two channels. Just like in the Belle II part, the horizontal line marks $N_{dec} = 3$ and thus the graph's intersections with it give the bounds of sensitivity for the detectors.

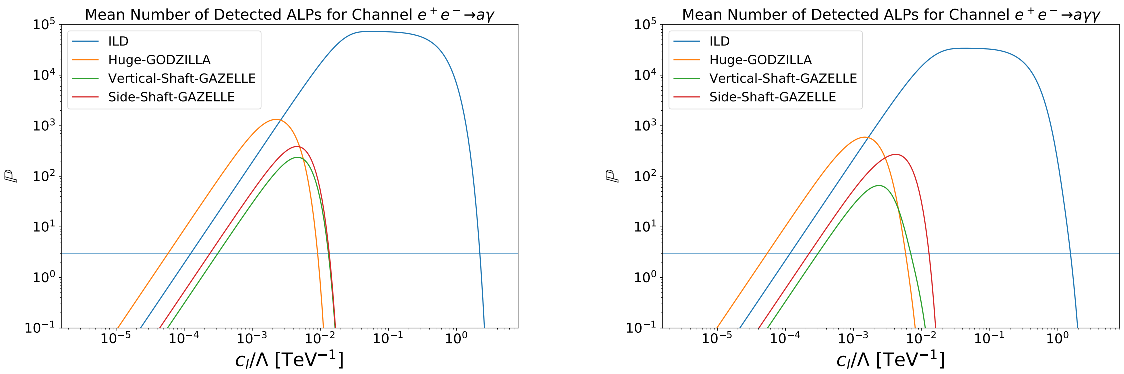

**(a)** $e^+e^- \to a\gamma$ **(b)** $e^+e^- \to Z\gamma \to a\gamma\gamma$

**Figure 4.8:** $N_{dec}$ as a function of $c_l/\Lambda$ for single channels

One finds that solely the lower bounds of sensitivity in $c_l/\Lambda$ for Huge-GODZILLA are smaller than the ones of the ILD in all channels. Therefore and as we have already concluded from the mean decay probabilities in Figure 4.7, merely Huge-GODZILLA achieves a gain in sensitivity for the detection of ALPs over the ILD. To quantify this gain, we determine the numeric values for the lower bounds $(c_l/\Lambda)_{min}$ for all detectors in all channels and summarize them in Table 4.2.

| | ILD | HG | VS | SS |
|---|---|---|---|---|
| $e^+e^- \to a\gamma$ | $1.25 \times 10^{-4}$ | $5.78 \times 10^{-5}$ | $3.12 \times 10^{-4}$ | $2.39 \times 10^{-4}$ |
| $e^+e^- \to ae^+e^-$ | $2.74 \times 10^{-4}$ | $1.28 \times 10^{-4}$ | $7.55 \times 10^{-4}$ | $5.47 \times 10^{-4}$ |
| $e^+e^- \to a\nu\nu$ | $2.86 \times 10^{-4}$ | $1.33 \times 10^{-4}$ | $7.04 \times 10^{-4}$ | $5.49 \times 10^{-4}$ |
| $e^+e^- \to Z\gamma \to a\gamma\gamma$ | $1.17 \times 10^{-4}$ | $5.38 \times 10^{-5}$ | $3.00 \times 10^{-4}$ | $2.23 \times 10^{-4}$ |

**Table 4.2:** Lower bounds of sensitivity $(c_l/\Lambda)_{\text{min}}$ [TeV$^{-1}$]

To have the direct comparison to the ILD, we determine the ratio in lower bounds $(c_l/\Lambda)^{\text{GAZELLE}}_{min}/(c_l/\Lambda)^{\text{ILD}}_{min}$. So a value smaller than one indicates a gain in sensitivity over the ILD for the detection of ALPs. These results are listed in Table 4.3.

| | ILD | HG | VS | SS |
|---|---|---|---|---|
| $e^+e^- \to a\gamma$ | 1 | 0.46 | 2.50 | 1.91 |
| $e^+e^- \to ae^+e^-$ | 1 | 0.47 | 2.76 | 2.00 |
| $e^+e^- \to a\nu\nu$ | 1 | 0.47 | 2.46 | 1.91 |
| $e^+e^- \to Z\gamma \to a\gamma\gamma$ | 1 | 0.46 | 2.57 | 1.91 |

**Table 4.3:** Fraction of lower bounds of sensitivity $(c_l/\Lambda)^{\text{GAZELLE}}_{\text{min}}/(c_l/\Lambda)^{\text{ILD}}_{\text{min}}$

Here, we see again that Huge-GODZILLA has an improved sensitivity for the detection of ALPs compared to the ILD while Vertical-Shaft-GAZELLE and Side-Shaft-GAZELLE offer no gains at all.

However, we make the same observation as in the Belle II part: the far detectors offer no gain in sensitivity by orders of magnitude. Merely an improved performance by a factor of $\sim 2$ is achieved for Huge-GODZILLA. This is due to the outstanding angular coverage and size of the ILD (see Section 4.1) and the thus already exceptionally good sensitivity for the detection of ALPs. Hence, it is questionable, whether the small gains of a far detector at the ILC would be worth the outstanding expenses and efforts to build such a far detector, especially a far-detector like Huge-GODZILLA with a $1\,\text{km}^2$-surface.

Although we now have already drawn conclusions about the possible gains in sensitivity of far detectors for the detection of ALPs at the ILC, we additionally want to present results in a more model-independent and general form. To do so, we compute $N_{dec}$ as a function of the ALP's decay-length $c\tau$ and the cross-section $\sigma$ of the production channel exactly as described in Section 2.2.
In Figure 4.9, $N_{dec}(c\tau, \sigma)$ is depicted in colormaps for all detectors and only for the channel $e^+e^- \to a\gamma$ because the colormaps of the other channels are all qualitatively identical. The black line in all plots marks $N_{dec} = 3$, such that the region on the inside corresponds to the region in parameter-space with $N_{dec} \geq 3$, i.e. the region where the detector is sensitive to the discovery of ALPs.

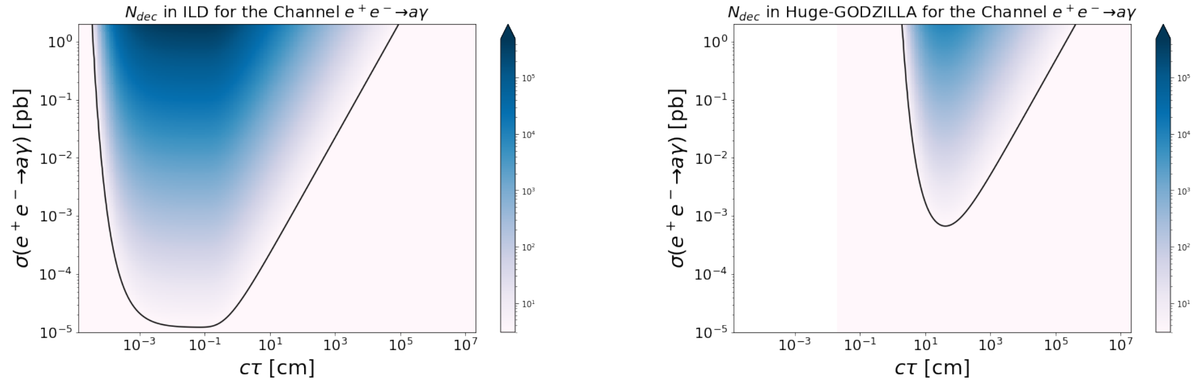

(a) ILD (b) Huge-GODZILLA

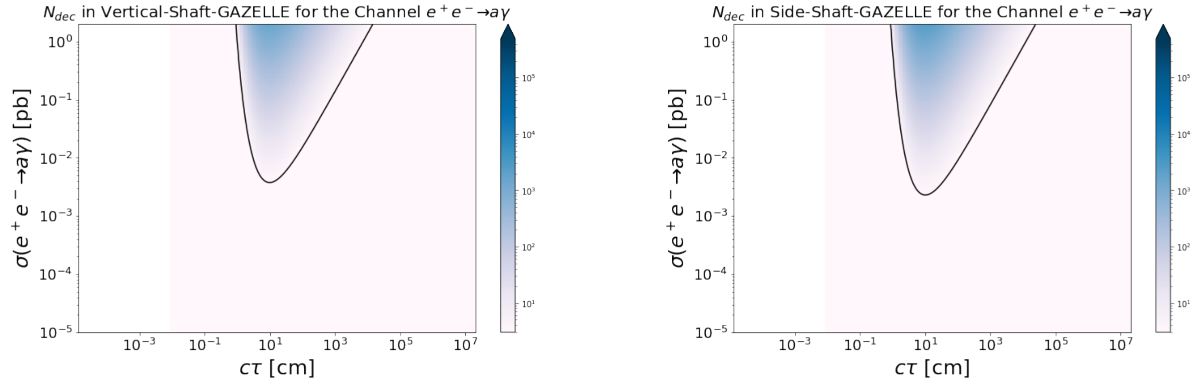

(c) Vertical-Shaft-GAZELLE (d) Side-Shaft-GAZELLE

**Figure 4.9:** $N_{dec}$ as a function of $c\tau$ and $\sigma$; the color corresponds to the value of $N_{dec}$

Two points are visible very clearly here. Firstly, the volume in parameter-space where the detector is sensitive is largest for the ILD, followed by Huge-GODZILLA and lastly Side-Shaft-GAZELLE and Vertical-Shaft-GAZELLE. Secondly, the sensitive regions of the three far detectors are shifted to larger decaylengths compared to the ILD. This of course is perfectly consistent with all observations in the preceding analysis above.
For a better comparison of the four detectors under study, we solely plot the $N_{dec} = 3$-contours without the colormaps of Figure 4.9 for all detectors and one single channel in one graph respectively. In Figure 4.10, this is done for the channels $e^+e^- \to a\gamma$ and $e^+e^- \to Z\gamma \to a\gamma\gamma$.

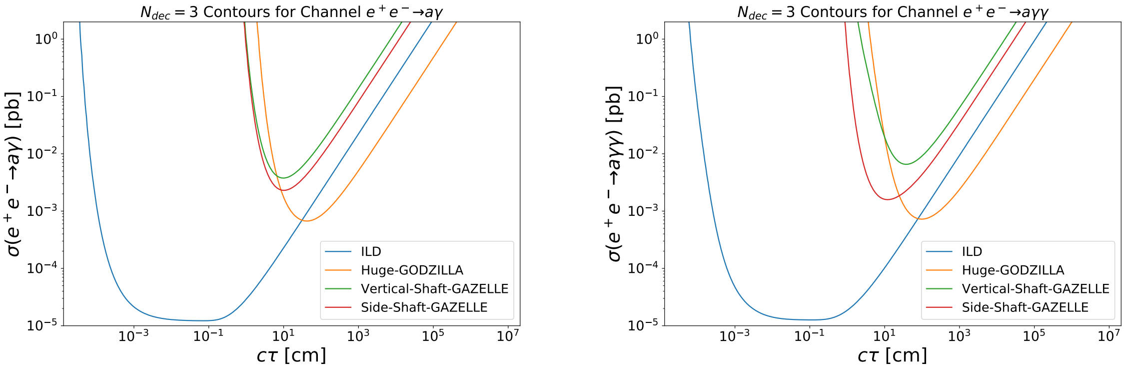

**(a)** $e^+e^- \to a\gamma$

**(b)** $e^+e^- \to Z\gamma \to a\gamma\gamma$

**Figure 4.10:** $N_{dec} = 3$-contours for single channels

It is visible here that Vertical-Shaft-GAZELLE and Side-Shaft-GAZELLE offer no gains in sensitivity. Their regions of sensitivity are entirely incorporated in the ILD's.
Huge-GODZILLA on the other hand exceeds the ILD's sensitivity for the detection of ALPs in a certain region of parameter-space for all channels. At $c\tau \approx 100\,\text{cm}$ and $\sigma \approx 10^{-3}\,\text{pb}$ Huge-GODZILLA's $N_{dec} = 3$-contour intersects the ILD's contour and from there on, i.e. going to larger $c\tau$ and $\sigma$, Huge-GODZILLA's performance exceeds the ILD. However, the improvement is again not of orders of magnitude which makes the construction of such an enormous detector rather unappealing.

In conclusion, for both parts of this analysis, considering firstly the 1D $(c_l/\Lambda)$-parameter-space and secondly the more general 2D $c\tau$-$\sigma$-parameter-space, we have seen that merely Huge-GODZILLA offers a gain in sensitivity for the detection of ALPs over the ILD. This gain however is not of orders of magnitude which does not justify the expenses and efforts of building a far detector of Huge-GODZILLA's dimensions. This result can be considered very positive because it implies that the ILD already is sensitive to the detection of long-lived particles and no expensive far detectors need to be constructed. If however a comprehensive backgrounds study indicates that there will be significant backgrounds in the ILD (in contrast to our zero-background assumption), far detectors could improve the sensitivity far more than concluded in this study. Then, the construction of a far detector could become sensible again.

# 5 Comparison of Belle II and ILC

In this chapter, we want to compare the sensitivity for the detection of ALPs of the CDC at Belle II and the ILD at the ILC, i.e. we want to compare the reach for the detection of long-lived ALPs at Belle II and ILC. On this basis we want to assess, which of the two experiments is better suited for an extensive ALP search.

To be able to compare the two experiments, we determine the mean number $N_{dec}$ of expected detected ALPs as a function of the two couplings $c_l/\Lambda$ and $c_{WW}/\Lambda$ for the CDC and the ILD exactly as described in Section 2.2. For the CDC, we do this solely for the 0.3 GeV ALP (as this is the only mass considered in the ILC analysis) and for the ILD, we consider all four production channels which have been studied in the chapters before. In Figures 5.1a-5.1e, the corresponding colormaps for $N_{dec}(c_l/\Lambda, c_{WW}/\Lambda)$ are depicted. As before, the black contour marks $N_{dec} = 3$ with $N_{dec} \geq 3$ on its inside.

In these plots two things are visible clearly. Firstly, the ILD covers a wider range in $c_l/\Lambda$ than the CDC (the lower "peak" is wider for the ILD than for the CDC) and secondly, the region of sensitivty is shifted to higher $c_{WW}/\Lambda$ for the CDC compared to the ILD but also the different channels within the ILD are slightly shifted relative to each other. We have already seen the coverage of a wider range in $c_l/\Lambda$ for the ILD in Section 4.4 and we concluded that this difference is due to the closer distance of the ILD to the interaction point. The shift in $c_{WW}/\Lambda$ is due to the differences in total number of produced ALPs. With increasing $c_{WW}/\Lambda$ the respective cross-section for the production of ALPs grows. For the different production channels at ILC, $e^+e^- \to a\gamma$ has the highest and $e^+e^- \to ae^+e^-$ has the lowest cross-section at equal $c_{WW}/\Lambda$. Therefore, a higher $c_{WW}/\Lambda$ is needed for the latter to obtain the same number of produced ALPs. The same argument applies for the shift for Belle II: the production process $e^+e^- \to B\overline{B}; B \to Ka$ has a far smaller cross-section than e.g. the process $e^+e^- \to a\gamma$ and therefore, higher $c_{WW}/\Lambda$ are needed to obtain the same number of detected ALPs. This even outweighs the 200 times higher integrated luminosity of the Belle II experiment.

To really see, which of the two experiments is more sensitive for the detection of ALPs, only the $N_{dec} = 3$-contours, which as we know border the regions of sensitivity, are plotted together in one graph in Figure 5.1f for Belle II and the four channels of ILC. We see that the region of sensitivity for Belle II is entirely included in the region of sensitivity of the ILC for the channels $e^+e^- \to a\gamma$ and $e^+e^- \to Z\gamma \to a\gamma\gamma$. The ILC covers a wider range in parameter-space and every ALP detected in Belle II would also be detected in the ILC. So despite the significantly higher integrated luminosity at Belle II, the ILC is better suited for an extensive ALP search.

One aspect however must still be noted. If we disregard the shift in $c_{WW}/\Lambda$, the sensitive region for Belle II is shifted to lower $c_l/\Lambda$ compared to the ILC due to the lower boosts the ALPs obtain at Belle II and the thus smaller decaylengths at equal $c_l/\Lambda$. So if the shift in $c_{WW}/\Lambda$ between ILC and Belle II was smaller, Belle II would exceed ILC's

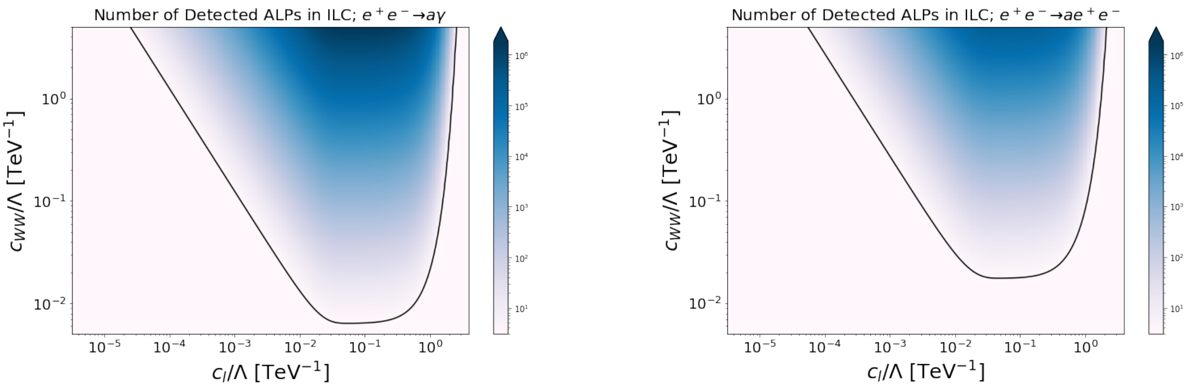

**(a)** ILC; $e^+e^- \to a\gamma$ **(b)** ILC; $e^+e^- \to ae^+e^-$

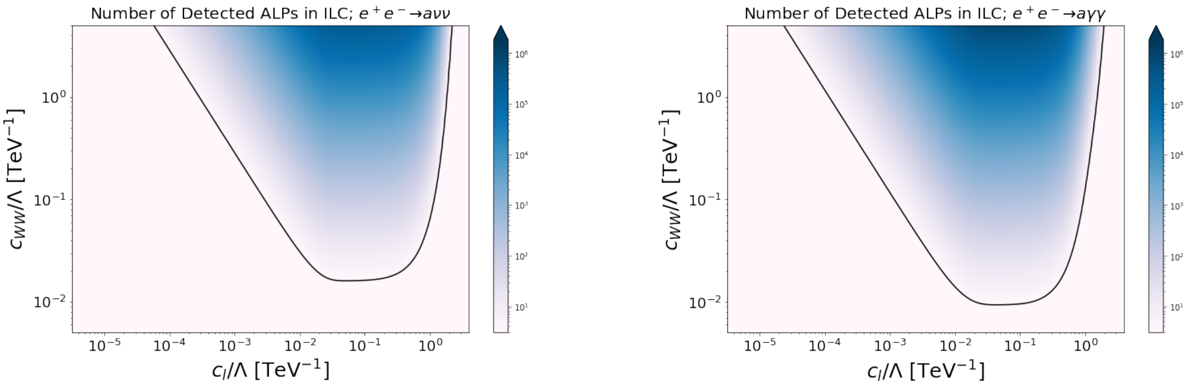

**(c)** ILC; $e^+e^- \to a\nu\nu$ **(d)** ILC; $e^+e^- \to Z\gamma \to a\gamma\gamma$

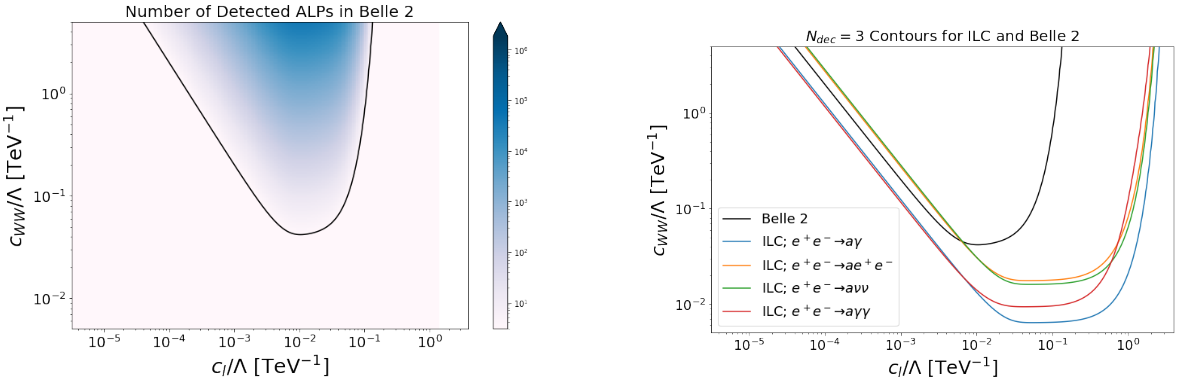

**(e)** Belle II **(f)** $N_{dec} = 3$-contours for Belle II and ILC

**Figure 5.1:** Comparison of $N_{dec}$ as a function of $c_l/\Lambda$ and $c_{WW}/\Lambda$ at ILC and Belle II; the color corresponds to the value of $N_{dec}$

sensitivity for small $c_l/\Lambda$. If for example the ILC does not achieve its goal for integrated luminosity, Belle II suddenly is more sensitive for the detection of ALPs in a certain region of parameter-space. Therefore, both experiments should feature a long-lived ALP search to cover the biggest possible region in parameter-space in all eventualities.

# 6 Conclusion

The overall goal of this study was to determine the possible gains in sensitivity for the detection of long-lived ALPs that far detectors can achieve over Belle II's and ILC's main detectors. Furthermore, a comparison of the two experiments and their main detectors was of special interest to be able to assess, at which collider an extensive ALP search is best conducted.

For the evaluation of the gain in sensitivity of far detectors, we proposed four different far-detector geometries for Belle II (see Section 3.1) and three different far-detector geometries for the ILC (see Section 4.1). The different geometries were designed to cover different ALP scenarios, i.e. different masses at Belle II and different production channels at the ILC.
In the actual detector analyses (see Section 3.4 and Section 4.4), we firstly determined the mean probabilities for ALPs to be detected by the detectors and then calculated the mean number of expected detected ALPs in the different detectors. From this, we could conclude that neither for Belle II nor for the ILC a significant gain in sensitivity over the experiment's main detectors could be achieved by any of the proposed far detectors. Some of the far detectors did offer improvements in sensitivity, however those improvements were relatively small and not of orders of magnitude. These small gains alone do not justify the expenses and efforts of constructing a far detector.
If however a long-lived ALP is discovered by some experiment, the construction of a far detector at Belle II and ILC will become more sensible because then, the small gains in sensitivity can result in higher precisions in the measurements of such a particle's properties.
The merely small gains in sensitivity of all the different far detectors highlight that Belle II's and ILC's main detectors already are highly sensitive to the detection of long-lived ALPs and that extensive searches for such particles should and can be conducted there even without additional far detectors.

For the comparison of Belle II's and ILC's sensitivity (see Chapter 5), we determined the mean number of expected detected ALPs in both main detectors as a function of the two fundamental couplings of our ALP model (see Section 2.1). Here, we saw that the ILC is sensitive for the detection of ALPs over a wider range in parameter-space and that Belle II does not offer further sensitivity in any regions of parameter-space. However, we also saw that Belle II can provide additional sensitivity if the ILC does not achieve its goal for integrated luminosity, which of course can happen for several reasons. Furthermore, results are always more reliable if two independent experiments conduct the same research and come to the same conclusions.
Therefore we conclude that extensive long-lived ALP searches should best be conducted at both colliders, the ILC and Belle II, to assure best possible sensitivity in all eventualities as well as reliable results in the case of a discovery.

# Bibliography

[1] Jonathan L. Feng et al. "ForwArd Search ExpeRiment at the LHC". In: *Physical Review D* 97.3 (Feb. 2018). ISSN: 2470-0029. DOI: `10.1103/physrevd.97.035001`. URL: `http://dx.doi.org/10.1103/PhysRevD.97.035001`.

[2] Anaïs Schaeffer; CERN. *LS2 Report: FASER is born.* Mar. 2021. URL: `https://home.cern/news/news/experiments/ls2-report-faser-born` (visited on 12/27/2021).

[3] Sascha Dreyer et al. *Physics reach of a long-lived particle detector at Belle II.* 2021. arXiv: `2105.12962 [hep-ph]`.

[4] R. D. Peccei and Helen R. Quinn. "CP Conservation in the Presence of Pseudoparticles". In: *Phys. Rev. Lett.* 38 (25 June 1977), pp. 1440–1443. DOI: `10.1103/PhysRevLett.38.1440`. URL: `https://link.aps.org/doi/10.1103/PhysRevLett.38.1440`.

[5] Steven Weinberg. "A New Light Boson?" In: *Phys. Rev. Lett.* 40 (4 Jan. 1978), pp. 223–226. DOI: `10.1103/PhysRevLett.40.223`. URL: `https://link.aps.org/doi/10.1103/PhysRevLett.40.223`.

[6] F. Wilczek. "Problem of Strong $P$ and $T$ Invariance in the Presence of Instantons". In: *Phys. Rev. Lett.* 40 (5 Jan. 1978), pp. 279–282. DOI: `10.1103/PhysRevLett.40.279`. URL: `https://link.aps.org/doi/10.1103/PhysRevLett.40.279`.

[7] Roberto D. Peccei. "The Strong CP Problem and Axions". In: *Axions* (2008), pp. 3–17. ISSN: 0075-8450. DOI: `10.1007/978-3-540-73518-2_1`. URL: `http://dx.doi.org/10.1007/978-3-540-73518-2_1`.

[8] David J. E. Marsh. *Axions and ALPs: a very short introduction.* 2017. arXiv: `1712.03018 [hep-ph]`.

[9] Howard Georgi, David B. Kaplan, and Lisa Randall. "Manifesting the Invisible Axion at Low-energies". In: *Phys. Lett. B* 169 (1986), pp. 73–78. DOI: `10.1016/0370-2693(86)90688-X`.

[10] Martin Bauer et al. "The low-energy effective theory of axions and ALPs". In: *Journal of High Energy Physics* 2021.4 (Apr. 2021). ISSN: 1029-8479. DOI: `10.1007/jhep04(2021)063`. URL: `http://dx.doi.org/10.1007/JHEP04(2021)063`.

[11] Martin Bauer, Matthias Neubert, and Andrea Thamm. "Collider probes of axion-like particles". In: *Journal of High Energy Physics* 2017.12 (Dec. 2017). ISSN: 1029-8479. DOI: `10.1007/jhep12(2017)044`. URL: `http://dx.doi.org/10.1007/JHEP12(2017)044`.

[12] M. B. Gavela et al. "Flavor constraints on electroweak ALP couplings". In: *The European Physical Journal C* 79.5 (Apr. 2019). ISSN: 1434-6052. DOI: `10.1140/epjc/s10052-019-6889-y`. URL: `http://dx.doi.org/10.1140/epjc/s10052-019-6889-y`.

[13] N. Gubernari, A. Kokulu, and D. van Dyk. “B →P and B →V form factors from B-meson light-cone sum rules beyond leading twist”. In: *Journal of High Energy Physics* 2019.1 (Jan. 2019). ISSN: 1029-8479. DOI: `10.1007/jhep01(2019)150`. URL: `http://dx.doi.org/10.1007/JHEP01(2019)150`.

[14] P.A. Zyla et al. “Review of Particle Physics”. In: *PTEP* 2020.8 (2020), p. 083C01. DOI: `10.1093/ptep/ptaa104`.

[15] Kazunori Akai, Kazuro Furukawa, and Haruyo Koiso. “SuperKEKB collider”. In: *Nuclear Instruments and Methods in Physics Research Section A: Accelerators, Spectrometers, Detectors and Associated Equipment* 907 (Nov. 2018), pp. 188–199. ISSN: 0168-9002. DOI: `10.1016/j.nima.2018.08.017`. URL: `http://dx.doi.org/10.1016/j.nima.2018.08.017`.

[16] J. P. Lees et al. “Search forB→K(*)¯and invisible quarkonium decays”. In: *Physical Review D* 87.11 (June 2013). ISSN: 1550-2368. DOI: `10.1103/physrevd.87.112005`. URL: `http://dx.doi.org/10.1103/PhysRevD.87.112005`.

[17] Howard Baer et al. *The International Linear Collider Technical Design Report - Volume 2: Physics*. 2013. arXiv: `1306.6352 [hep-ph]`.

[18] Jolanta Brodzicka et al. *Physics Achievements from the Belle Experiment*. 2012. arXiv: `1212.5342 [hep-ex]`.

[19] Deutsche Elektronen-Synchrotron DESY. *Super KEKB and Belle II*. URL: `https://www.belle2.org/project/super_kekb_and_belle_ii/` (visited on 11/02/2021).

[20] T. Abe et al. *Belle II Technical Design Report*. 2010. arXiv: `1011.0352 [physics.ins-det]`.

[21] 2016 Belle II Experiment. *The Belle II Experiment - The Detector*. URL: `https://belle2.jp/detector/` (visited on 11/03/2021).

[22] Deutsche Elektronen-Synchrotron DESY. *Archives*. URL: `https://www.belle2.org/archives/` (visited on 11/04/2021).

[23] David Curtin and Michael E. Peskin. “Analysis of long-lived particle decays with the MATHUSLA detector”. In: *Physical Review D* 97.1 (Jan. 2018). ISSN: 2470-0029. DOI: `10.1103/physrevd.97.015006`. URL: `http://dx.doi.org/10.1103/PhysRevD.97.015006`.

[24] Ties Behnke et al. *The International Linear Collider Technical Design Report - Volume 1: Executive Summary*. 2013. arXiv: `1306.6327 [physics.acc-ph]`.

[25] Chris Adolphsen et al. *The International Linear Collider Technical Design Report - Volume 3.II: Accelerator Baseline Design*. 2013. arXiv: `1306.6328 [physics.acc-ph]`.

[26] Ties Behnke et al. *The International Linear Collider Technical Design Report - Volume 4: Detectors*. 2013. arXiv: `1306.6329 [physics.ins-det]`.

# List of Figures

# List of Tables

# Acknowledgements

I would like to thank Susanne and Ruth for all the guidance, advice, the time they took for explanations and discussions and of course for the opportunity to work in their group. It was a pleasure working with you two on this highly interesting subject. Special thanks also goes to Torben who answered all my questions about Tsukuba Hall and possible detector geometries at Belle II. Lastly, I have to thank Ruth (again) and Sander for reading this thesis and giving good feedback before submission.

# Erklärung

Ich versichere, dass ich diese Arbeit selbstständig verfasst und keine anderen als die angegebenen Quellen und Hilfsmittel benutzt habe.

Heidelberg, den 31.12.2021, Finn Tillinger

F. Tillinger